

# Intrinsically chiral ferronematic liquid crystals: an inversion of the helical twist sense at the chiral nematic – chiral ferronematic phase transition

Damian Pocięcha, Rebecca Walker,<sup>[b]</sup> Ewan Cruickshank,<sup>[b]</sup> Jadwiga Szydłowska,<sup>[a]</sup> Paulina Rybak,<sup>[a]</sup> Anna Makal,<sup>[a]</sup> Joanna Matraszek,<sup>[a]</sup> Joanna M. Wolska,<sup>[a]</sup> John M.D. Storey,<sup>[b]</sup> Corrie T. Imrie<sup>[b]</sup> and Ewa Gorecka<sup>\*[a]</sup>

[a] Department of Chemistry, University of Warsaw, Żwirki i Wigury 101, 02-089 Warsaw, Poland

[b] Department of Chemistry, University of Aberdeen, Old Aberdeen AB24 3UE, U.K.

**KEYWORDS:** *nematic, ferroelectric, chirality*

**ABSTRACT:** Strongly dipolar mesogenic compounds with a chiral center located in a lateral alkyl chain were synthesized, and shown to form the ferroelectric nematic phase. The presence of molecular chirality induced a helical structure in both the N\* and N<sub>F</sub>\* phases, but with opposite helix sense in the two phases. The relaxation frequency of the polar fluctuations is only weakly affected by helical structure, it was found to be slightly lower for the chiral N<sub>F</sub>\* phase than for its achiral, non-branched counterpart with the same lateral chain length.

## ■ INTRODUCTION

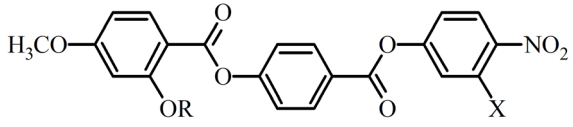
The recent discovery of the ferroelectric nematic or ferronematic, N<sub>F</sub>, phase [1-7] is of profound fundamental and technological importance, and heralds a new field of scientific endeavour in condensed matter, complementing the extensively studied solid ferroelectrics. Previously, polar order in soft matter had been observed only in phases with some degree of positional order, smectic [8-10] and columnar phases [11] or in lyotropic nematics made of polymers [12]. In the conventional nematic, N, phase the long axes of the rod-like molecules are more or less aligned in the same direction, along the director, and their centres of mass are randomly distributed. The director is denoted by the unit vector **n** having inversion symmetry such that **n** = -**n**, and hence, the phase is non-polar. Chiral systems show the chiral nematic phase, N\*, in which the molecular chirality causes the director to form a helix. The sense of the helix is pre-determined by the sense of molecular chirality and molecular conformation [13]. At the molecular level the N and N\* phases are indistinguishable. The N<sub>F</sub> phase was predicted over a century ago, in which the molecular dipole moments align in the same direction, *i.e.* **n** ≠ -**n**, giving a ferroelectric fluid [14]. Polar order in liquids is an absolutely fundamental issue not only in chemistry and physics but may also have far reaching implications in biological sciences. It is widely believed that chirality holds the key to an understanding of the origins of life and liquid crystals are ideal systems to study chirality, its origins and chirality propagation. Some forty years ago, it was predicted that the ferroelectric nematic phase, in order to reduce electrostatic energy, will twist giving a polar N\* phase with **n** ≠ -**n** [15], the spontaneous chirality being controlled through steric and electrostatic interactions between achiral molecules. Such a mechanism may have fundamental implications for the origins of chirality. This spontaneous chirality has not been observed in the very small number of ferronematogens studied to date, but does pose the fascinating question, how will an intrinsically chiral ferronematogen behave? So far the only chiral system

reported comprises an achiral ferronematogen doped with a chiral additives [16-18], and although such systems have much merit, the interpretation of their behaviour at a molecular level, both experimentally and theoretically, is made significantly more complex by their bicomponent nature. To better understand how intrinsic molecular chirality affects the formation of the N<sub>F</sub> phase, here for the first time we report the synthesis and characterization of intrinsically chiral ferroelectric nematogens, and compare their properties to those of structurally similar achiral materials. These compounds are based on the prototype ferroelectric nematogen, RM-734 [4], here referred to as **I-1**, and their structures and transitional properties are shown in Table 1. The chiral center has been introduced into a laterally attached alkyl chain at the third atom away from the mesogenic core. The single crystal x-ray diffraction data for compounds **I-3** and **I-4**, the only materials for which good quality crystals could be obtained, reveal that in the crystal lattice (monoclinic *P*2<sub>1</sub>/*c* space group) the lateral chains are in a fully extended conformation, and the electric dipoles of neighboring molecules are arranged in an antiparallel fashion (see SI).

## ■ RESULTS AND DISCUSSION

The homologous series **I-*m***, in which the lateral *n*-alkyl chain increases from methyl to hexyl (*m*=1-6) was studied to guide the design of the target chiral ferroelectric nematogen, compound **I-4\***. All the homologues show monotropic nematic and ferronematic phases, except for the methyl member, **I-1**, for which the nematic phase was enantiotropic (Table 1). It must be noted, however, that all these materials readily supercool to temperatures far below their melting points. Indeed, in some cases the monotropic N<sub>F</sub> phase was stable at room temperature for hours prior to crystallizing. As expected, the Iso-N and N-N<sub>F</sub> transition temperatures decrease as the lateral alkyl chain is extended, and the effect on the clearing temperature is more pronounced. As a result, the temperature range of the higher temperature nematic phase decreases with increasing lateral chain length (inset in Fig. 1).

Table 1. Molecular structures and transition temperatures obtained from DSC scans (heating and cooling, 10 K/min). The associated enthalpy changes are given in brackets (J/g).

			
	R	X	
I-1	CH <sub>3</sub>	H	Cr 139.0 (80.5) N 188.0 (1.5) Iso Iso 187.0 (1.5) N 130.7 (1.5) N <sub>F</sub>
I-2	C <sub>2</sub> H <sub>5</sub>	H	Cr 159.0 (131.0) Iso Iso 131.0 (1.9) N 106.0 (3.6) N <sub>F</sub>
I-3	C <sub>3</sub> H <sub>7</sub>	H	Cr 146.0 (98.9) Iso Iso 96.2 (1.1) N 84.6 (2.9) N <sub>F</sub>
I-4	C <sub>4</sub> H <sub>9</sub>	H	Cr 141.0 (97.8) Iso Iso 74.6 (0.6) N 64.8 (1.8) N <sub>F</sub>
I-5	C <sub>5</sub> H <sub>11</sub>	H	Cr 130.4 (108.2) Iso Iso 60.0 (1.0) N 52.7 (2.2) N <sub>F</sub>
I-6	C <sub>6</sub> H <sub>13</sub>	H	Cr 101.0 (73.8) Iso Iso 50.1 (0.8) N 43.6 (1.3) N <sub>F</sub>
I-4*	CH <sub>2</sub> CH(CH <sub>3</sub> )C <sub>2</sub> H <sub>5</sub>	H	Cr 140.0 (92.1) Iso Iso 56.1 (-) N* 54.8 (3.5 <sup>†</sup> ) N <sub>F</sub> *
II-6	C <sub>6</sub> H <sub>13</sub>	F	Cr 77.0 (75.5) Iso Iso 47.8 (4.2) N <sub>F</sub>
II-4*	CH <sub>2</sub> CH(CH <sub>3</sub> )C <sub>2</sub> H <sub>5</sub>	F	Cr 111.0 (74.8) Iso Iso 54.9 (5.2) N <sub>F</sub> *

<sup>†</sup> the peaks corresponding to the N\*-N<sub>F</sub>\* and Iso-N\* transitions are not well resolved.

Both transition temperatures appear to be approaching limiting values on increasing chain length, and for T<sub>Nl</sub> such behavior is normally attributed to the alkyl chain adopting conformations in which it lies along the long molecular axis and thus its elongation does not disturb the parallel arrangement of neighboring molecules [19]. The overall decrease in both transition temperatures clearly correlates with a decreasing molecular shape anisotropy, as evidenced by the optical birefringence ( $\Delta n$ ) measurements (Fig. 1). Specifically,  $\Delta n$  strongly decreases in both the N and N<sub>F</sub> phases as the lateral chain is increased. In addition, as the temperature range of the N phase preceding the N<sub>F</sub> phase decreases with increasing  $m$ , the N-N<sub>F</sub> transition becomes more strongly first order in character, and is accompanied by a larger jump in  $\Delta n$  (Fig. 1). Hence, a stronger increase in the order parameter at this transition is detected. A further decrease in the molecular anisotropy by introducing an F atom ortho to the terminal nitro group (compounds II) destabilized the N phase completely, and a direct Iso-N<sub>F</sub> phase transition was observed for compound II-6. Branching the lateral chain by introducing a chiral carbon atom (*cf.* compounds I-4 and I-4\*) decreases the nematic phase stability even further, both the N\*-N<sub>F</sub>\* and Iso-N\* phase transition temperatures for the chiral compound I-4\* are lower than for its unbranched counterpart I-4 by 10 and 19 K, respectively.

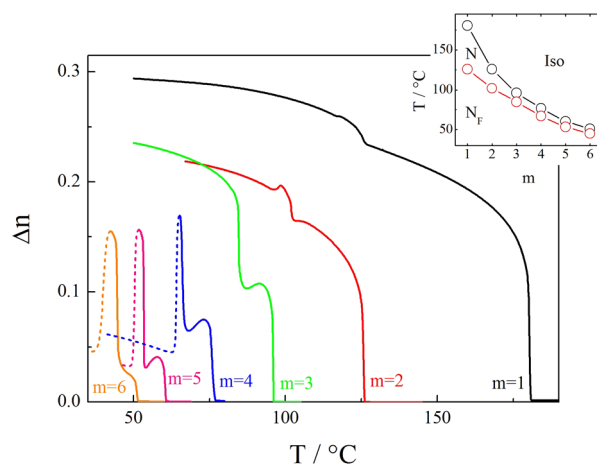


Figure 1. Optical birefringence measured with green light (532 nm) as a function of temperature for homologues I- $m$ ; a decrease in molecular anisotropy results in smaller values of the birefringence. At the N-N<sub>F</sub> phase transition, there is a step-wise increase of birefringence due to the growing orientational order parameter. A decrease in measured retardation observed in the N<sub>F</sub> phase a few degrees below the transition from the N phase, for homologues I-4, I-5 and I-6 is due to the formation of twisted states induced by interactions with the antiparallel rubbed polymer layers at the cell surfaces; note that the data in this range, presented as dashed lines, do not represent actual  $\Delta n$  values.

Introducing the F substituent ortho to the terminal nitro group in the mesogenic core (compound II-4\*) further destabilized the N\* phase revealing a direct Iso-N<sub>F</sub>\* transition with a clearing temperature similar to the non-substituted chiral material I-4\*. It should be noted that compound I-4\* was recently mentioned in ref. 17, but its mesogenic properties were overlooked, and the material was used only as a chiral dopant. Molecular chirality introduces a twist deformation of the director (*i.e.* the averaged local direction of the long molecular axes) field and both nematic phases acquire a helical structure. The helical pitch in the N<sub>F</sub>\* phase could be deduced from its optical texture. Thus, whereas fast cooling in a few micron thick cell treated for planar anchoring resulted in the uniform orientation of the helix perpendicular to the cell surface (Fig. S5), slow cooling of the sample resulted in a well-defined fingerprint texture, with a periodicity of  $\sim 2.5 \mu\text{m}$  and  $\sim 5 \mu\text{m}$  for compounds I-4\* and II-4\*, respectively (Fig. S5). The helical structure of the director field results in the pronounced optical activity of the phases. For wavelengths ( $\lambda$ ) in the visible range the optical rotatory power (ORP) is in the Mauguin regime (for  $\lambda < np$ ,  $n$  being the average refractive index and  $p$  the helical pitch length), and therefore, shows a linear dependence on the helical pitch length according to: 
$$\text{ORP} = \frac{\pi \Delta n^2 p}{4\lambda^2}$$
 [20, 21], the formula is valid for pitch length up to few optical wavelengths. For green light (532 nm) for compound I-4\*, the ORP was  $\sim 8 \text{ deg. } \mu\text{m}^{-1}$  in the N<sub>F</sub>\* phase far below the N\*-N<sub>F</sub>\* transition and  $\sim 3 \text{ deg. } \mu\text{m}^{-1}$  in the N\* phase (Fig. 2); assuming that the birefringence of the nematic phases is similar to that of the achiral counterpart I-4 (molecules of both compounds share the same mesogenic core, and optical birefringence depends mainly on anisotropy of stiff molecular part), and taking into account the difference in  $\Delta n$  between the

nematic and polar nematic phases, the helical pitch calculated from the ORP values in both the  $N^*$  and  $N_F^*$  phases is  $\sim 2\text{-}3\ \mu\text{m}$ .

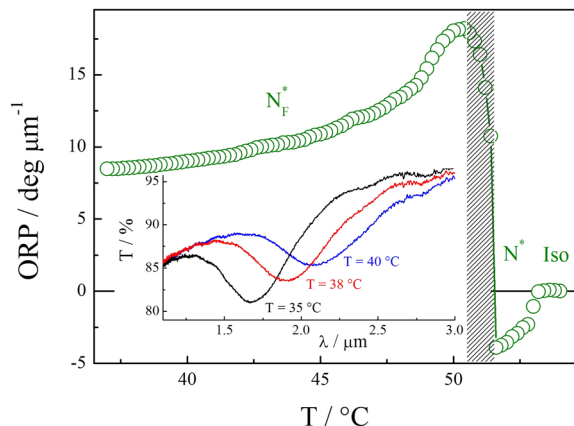


Figure 2. Optical rotatory power (ORP) measured in a 6- $\mu\text{m}$ -thick cell with green (532 nm) light for compound **I-4\***. The change in the sign of ORP at the  $N^*$ - $N_F^*$  transition indicates a change of the helical twist sense. Dashed area corresponds to the temperature range near the phase transition in which dynamic changes of the optical texture take place, which disturb precise ORP determination. In the inset, the dependence of transmittance vs. wavelength at chosen temperatures in the  $N_F^*$  phase, showing the selective reflection band (corresponding to half pitch).

Direct spectroscopic measurements in the  $N_F^*$  phase confirmed that the band gap is in the IR range (Fig. 2 inset). Interestingly, the ORP has opposite signs in the  $N_F^*$  and  $N^*$  phases (Fig. 2), indicating that the helices in these phases are of opposite twist sense. On approaching the  $N^*$  phase, the ORP increases in the  $N_F^*$  phase, indicating helix elongation before changing its sign in the  $N^*$  phase. Also, circular dichroism (CD) measurements clearly show the inversion of helix sense. The signal corresponding to the  $n\text{-}\pi^*$  transition (at  $\sim 360\ \text{nm}$ ) of the carbonyl group was monitored as a function of temperature, and it is well-known that the carbonyl CD spectrum is a very sensitive marker of the chiral environment [22]. The CD signal is enhanced and positive in the  $N^*$  phase due to the helix formation, while in the  $N_F^*$  phase its sign changes to negative and the signal becomes stronger (Fig. S8). The helix inversion might result from conformational changes of molecules [13] or from different interactions between neighboring molecules when they are in random up-down correlations in the  $N^*$  phase as opposed to when the head-tail orientation equivalence is broken in the  $N_F^*$  phase. It is worth noting that this effect is similar to that observed for chiral smectic C phases, when the helix changes sign upon transition from the synclinal  $\text{SmC}^*$  to anticlinal  $\text{SmC}_A^*$  phase [23, 24]. For compound **II-4\*** the value of ORP saturates at  $\sim 15\ \text{deg}/\mu\text{m}$  far from the phase transition, and the helix is also in IR range (Fig. S7). The CD signal over all the temperature range of the mesophase is negative (Fig. S8).

The spontaneous electric polarization was measured for both, chiral and non-chiral analogues, however due to recrystallization of the sample in the case of the non-chiral material **I-4** it was not possible to record full temperature dependence. Nevertheless, several degrees below the transition to the  $N_F$  phase, the values of electric polarization were found comparable for both compounds:  $\sim 5.3\ \mu\text{C cm}^{-2}$  and  $\sim 4.8\ \mu\text{C cm}^{-2}$  for **I-4** and **I-4\***, respectively. For the chiral

material, a critical decrease of spontaneous polarization in the  $N_F^*$  phase was observed on approaching the  $N_F^*$  -  $N^*$  phase transition (Fig. S6).

Dielectric spectroscopy measurements gave information on the polarization vector fluctuations, and were performed in glass cells with transparent ITO or gold electrodes, without polymer aligning layers to avoid the effect of polymer layer capacitance [25] given that the capacitance of the thin polymer layer becomes comparable to the capacitance of the tested compound layer for materials with giant dielectric permittivity, as well as to avoid the formation of twist states induced by interactions with the rubbed surfaces in the  $N_F$  phase. In such cells nematic phases adopted preferably planar configuration, however without uniform direction of the long molecular axis. In the  $N$  phase above the ferroelectric phase, a weak dielectric mode is found, the strength of which increases and frequency decreases on cooling, such a softening of the mode is a characteristic of an increasing correlation length of the polar fluctuations in a non-polar (paraelectric) phase [26].

For all the compounds in the  $N_F$  phase, dielectric spectroscopy shows a single, very strong dielectric relaxation mode (Fig. 3, Figs. S9-S16) which results from a combination of amplitude fluctuation (*i.e.*, collective changes of the magnitude of the polarization vector that are pronounced close to the  $N_F$ - $N$  phase transition) and phase fluctuations (*i.e.*, collective changes of the direction of the polarization vector).

The contribution of the amplitude mode is significant only in close vicinity of the transition temperature, at lower temperatures it is obscured by much stronger phason fluctuations. The relaxation frequency of this mode depends on the material, namely it decreases with elongation of the lateral chain, from  $\sim 1\ \text{kHz}$  for **I-1** [25] to  $\sim 50\ \text{Hz}$  for **I-6** (a few degrees below the  $N$ - $N_F$  phase transition). As the temperature is lowered, a clear cross over is found from a critical decrease, predominant near to the transition to the paraelectric nematic phase, to a decrease driven by non-critical Arrhenius-type behavior,  $f_r \sim e^{-\frac{E_a}{kT}}$ , deep in the  $N_F$  phase [26]. Far from the phase transition temperature, the relaxation frequency decrease is mainly due to the increasing rotational viscosity of polarization vector fluctuations. The activation energy for ferroelectric fluctuations in the  $N_F$  phase was determined from the relaxation frequency vs.  $1/T$  dependence (inset Fig. 3c), and is comparable in value ( $\sim 100\ \text{kJ mol}^{-1}\ \text{K}^{-1}$ ) for all the compounds. When comparing the dielectric properties of the chiral versus achiral materials, the relaxation frequency in the achiral compound (**I-4**) is slightly larger than in its chiral counterpart (**I-4\***), but the temperature dependence of the mode parameters is very similar. In both compounds, the fluctuations could be easily suppressed by a weak bias field, just  $\sim 0.2\ \text{V}\ \mu\text{m}^{-1}$  is sufficient. For chiral compound **II-4\***, in which the F atom was substituted at ortho position to the nitro group (Tab. 1) and a direct Iso- $N_F^*$  transition is observed, the dielectric mode relaxation frequency is slightly higher than in its chiral non-substituted counterpart **I-4\***. In general, the presence of the chiral center in the lateral chain caused only a small difference in the dielectric mode frequency in the  $N_F$  phase. No pronounced influence of the helical structure on the phason fluctuations were detected for the chiral material. This is in contrast to what is usually reported for chiral smectic

phases, for which the elongation of the helix pitch significantly decreases the relaxation frequency of the phason mode [27].

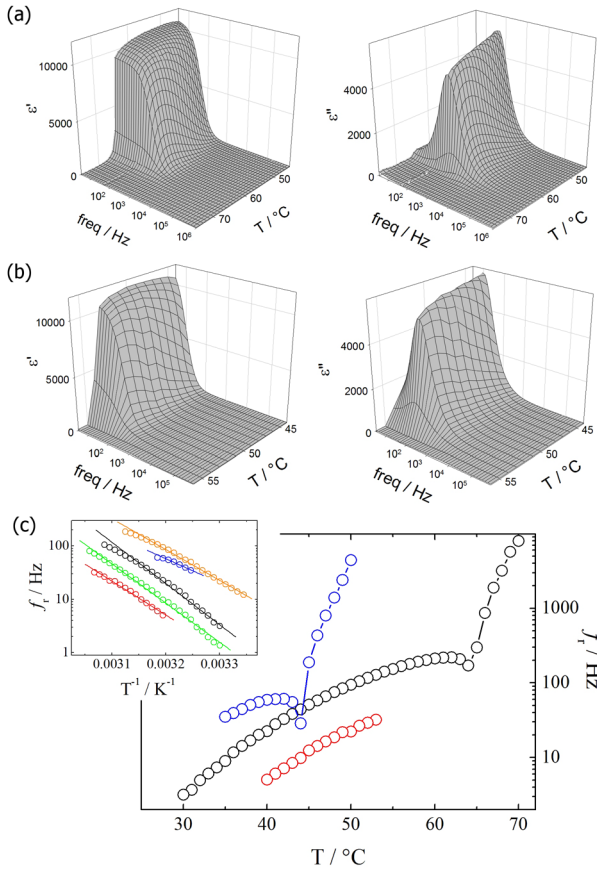


Figure 3. Real and imaginary parts of the dielectric permittivity measured vs. temperature and frequency, in 10- $\mu$ m-thick cells with ITO electrodes and no aligning layers, for (a) **I-4** and (b) **I-4\***. (c) Temperature dependence of relaxation frequency for **I-4** (black), **I-4\*** (red) and **II-6** (blue), measured in 10- $\mu$ m-thick cell with Au electrodes and no aligning layers. In the inset,  $1/T$  dependence of relaxation frequency in the  $N_F$  phase a few degrees below the phase transition from the  $N$  phase; the comparable slopes of the curves show similar activation energies of fluctuations for the studied materials. It is 148  $\text{kJ mol}^{-1} \text{K}^{-1}$  for **I-4** (black), 121  $\text{kJ mol}^{-1} \text{K}^{-1}$  for **I-4\*** (red), 87  $\text{kJ mol}^{-1} \text{K}^{-1}$  for **I-6** (blue), 110  $\text{kJ mol}^{-1} \text{K}^{-1}$  for **II-6** (orange), and 141  $\text{kJ mol}^{-1} \text{K}^{-1}$  for **II-4\*** (green).

In addition, second harmonic generation (SHG) measurements were performed to confirm the existence of polar order (Fig. 4). The  $N$  and crystal phases were SHG silent, and no signal was also observed in the  $N^*$  phase despite it being allowed by the non-centrosymmetric helical structure of the cholesteric phase. In contrast, in the  $N_F$  and  $N_F^*$  phases, a strong SHG signal was found (Fig. 4a).

It would appear that the detected SHG signal originates from the long-range ordering of the electric dipoles. For materials showing a direct  $N_F$ -Iso phase transition, the appearance of the signals is abrupt. For both **I-4** and **I-4\***, the SHG signal was sufficiently strong to be detected with the naked eye in relatively thin, 20  $\mu\text{m}$  cells (upon irradiation with  $\lambda=1064 \text{ nm}$ , pulse duration 9 ns and  $\sim 2 \text{ mJ}$  in the pulse), which agrees well with previous reports on strong SHG activity of ferroelectric phase [28, 29]. In an external electric field, which causes the

reorientation of the electric polarization in the direction of light propagation, the SHG signal disappears, and switching off the field restores the SHG signal, as in the cell with strong planar anchoring, the polarization vector re-adopts the direction perpendicular to the light propagation direction, in the  $N_F^*$  phase the helix is restored (Fig. 4b). Restoring of SHG signal is relatively slow, which might be related to high viscosity of our material.

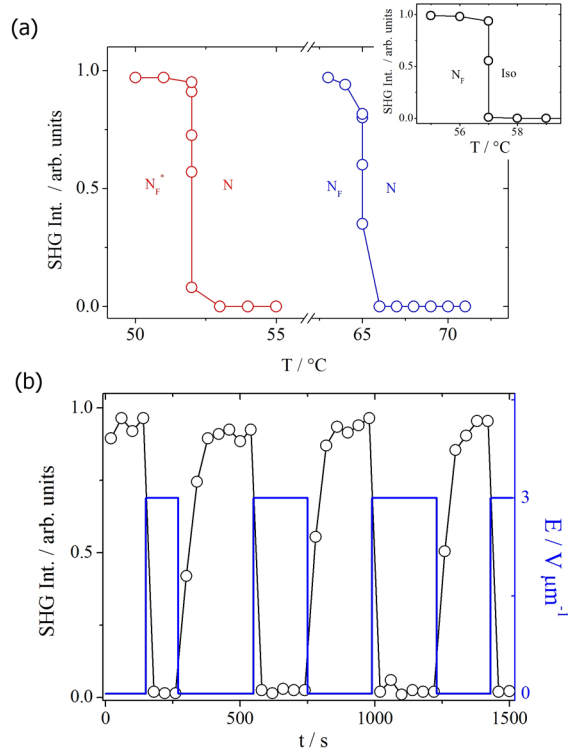


Figure 4. Relative intensity of the SHG signal versus temperature for (a) **I-4** (blue) and **I-4\*** (red) compounds; in the inset, data for compound **II-4\*** which shows an Iso- $N_F^*$  transition. (b) The modulation of the SHG signal intensity in a planar 5- $\mu\text{m}$ -thick cell for compound **I-4\*** in the  $N_F^*$  phase upon application of an electric field (blue line) normal to the cell surface; a high intensity SHG signal is observed in the switched-off state and low intensity in the switched on-state, due to the orientation of molecules along the light propagation direction.

## CONCLUSION

Intrinsically chiral compounds that form the ferroelectric nematic,  $N_F^*$ , phase were investigated and their properties compared with those of their achiral counterparts. The chiral auxiliary was placed ortho to the ester link in the methoxy-terminated phenyl ring. It is known that when placed in a flexible chain, the further the chiral center is from the mesogenic core, the less the transition temperatures are reduced, however, the weaker the twisting ability of the molecule. For the compounds studied here, this molecular modification decreased the transition temperatures, resulting in lower temperature ranges over which the  $N$  and  $N_F$  phases are observed than for non-branched compounds. The helical structure in the  $N^*$  and  $N_F^*$  phases have a few-micron-long pitch, but interestingly with opposite twist sense in these

phases. This inversion is evident in both the ORP as well as in the CD signal of the carbonyl group (that is a sensitive marker of chiral environment) which change sign at the  $N^*-N_F^*$  transition. The dielectric relaxation properties were mainly influenced by the rotational viscosity of the material such that lengthening and branching the lateral chain makes the fluctuations of the spontaneous polarization vector slower. The dielectric relaxation mode frequency for the chiral compounds was systematically lower by 50 Hz than for its achiral non-branched counterparts with the same lateral chain length, the activation energy for phason fluctuations was similar for all compounds. Strong SHG properties were found for both chiral and achiral  $N_F$  phases, confirming their polar character.

## ■ AUTHOR INFORMATION

### Corresponding Author

\* gorecka@chem.uw.edu.pl

### Author Contributions

The manuscript was written through contributions of all authors.

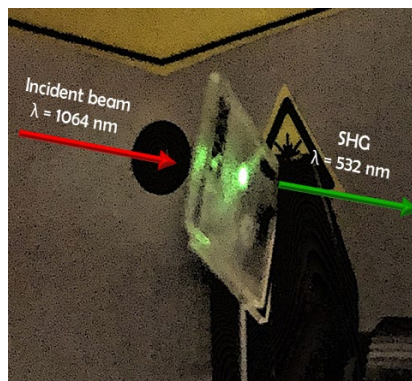
## ■ ACKNOWLEDGMENTS

The research was supported by the National Science Centre (Poland) under the grant no. 2016/22/A/ST5/00319. C.T.I. and J.M.D.S. acknowledge the financial support of the Engineering and Physical Sciences Research Council [EP/V048775/1].

## ■ REFERENCES

- (1) Mandle, R. J.; Cowling, S. J.; Goodby, J. W. Rational Design of Rod-Like Liquid Crystals Exhibiting Two Nematic Phases *Chem Eur J* **2017**, *23*, 14554.
- (2) Mertelj, A.; Cmok, L.; Sebastián, N.; Mandle, R. J.; Parker, R. R.; Whitwood, A. C.; Goodby, J. W.; Čopič, M. Splay Nematic Phase *Phys Rev X* **2018**, *8*, 041025.
- (3) Li, J.; Nishikawa, H.; Kougo, J.; Zhou, J.; Dai, S.; Tang, W.; Zhao, X.; Hisai, Y.; Huang, M.; Aya, S. Development of ferroelectric nematic fluids with giant- $\epsilon$  dielectricity and nonlinear optical properties *Sci Adv* **2021**, *7*, eabf5047.
- (4) Mandle, R. J.; Cowling, S. J.; Goodby, J. W. Structural variants of RM734 in the design of splay nematic materials *Liq Cryst* **2021**, *48*, 1780.
- (5) Manabe, A.; Bremer, M.; Kraska, M. Ferroelectric nematic phase at and below room temperature *Liq Cryst* **2021**, *48*, 1079.
- (6) Chen, X.; Korblova, E.; Dong, D.; Wei, X.; Shao, R.; Radzihovsky, L.; Glaser, M. A.; Maclennan, J. E.; Bedrov, D.; Walba, D. M.; Clark, N. A. First-principles experimental demonstration of ferroelectricity in a thermotropic nematic liquid crystal: Polar domains and striking electro-optics *PNAS*, **2020**, *117*, 14021.
- (7) Sebastián, N.; Cmok, L.; Mandle, R. J.; de la Fuente, M. R.; Drevenšek Olenik, I.; Čopič, M.; Mertelj, A. Ferroelectric-Ferroelastic Phase Transition in a Nematic Liquid Crystal *Phys Rev Lett* **2020**, *124*, 037801.
- (8) Takezoe, H.; Gorecka, E.; Čepič, M. Antiferroelectric liquid crystals: Interplay of simplicity and complexity *Rev Mod Phys* **2010**, *82*, 897.
- (9) Reddy, R. A.; Tschierske, C. Bent-core liquid crystals: polar order, superstructural chirality and spontaneous desymmetrisation in soft matter systems *J Mater Chem* **2006**, *16*, 907.
- (10) Takezoe, H.; Takanishi, Y. Bent-Core Liquid Crystals: Their Mysterious and Attractive World *Jap J App Phys* **2006**, *45*, 597.
- (11) Scherowsky, G.; Chen, X. H. Ferroelectric switching in columnar phases of novel chiral discotic liquid crystals *J Mater Chem* **1995**, *5*, 417.
- (12) Park, B.; Kinoshita, Y.; Takezoe, H.; Watanabe, J. Ferroelectricity in the Lyotropic Cholesteric Phase of Poly L-Glutamate *Jap J App Phys* **1998**, *37*, L136.
- (13) Loubser, C.; Wessels, P. L.; Styring, P.; Goodby, J. W. Helix inversion in the chiral nematic phase of a ferroelectric liquid crystal containing a single chiral centre *J Mater Chem* **1994**, *4*, 71.
- (14) Born, M. Elektronentheorie des natürlichen optischen Drehungsvermögens isotroper und anisotroper Flüssigkeiten *Annalen der Physik* **1918**, *360*, 177.
- (15) Khachatryan, A. G. Development of helical cholesteric structure in a nematic liquid crystal due to the dipole-dipole interaction *J Phys Chem Sol* **1975**, *36*, 1055.
- (16) Nishikawa, H.; Araoka, F. A New Class of Chiral Nematic Phase with Helical Polar Order *Adv Mat* **2021**, *33*, 2170270.
- (17) Zhao, X.; Zhou, J.; Li, J.; Kougo, J.; Wan, Z.; Huang, M. A.-O.; Aya, S. A.-O. Spontaneous helielectric nematic liquid crystals: Electric analog to helimagnets. *PNAS*, **2021**, *118*, e2111101118.
- (18) Feng, C.; Saha, R.; Korblova, E.; Walba, D.; Sprunt, S. N.; Jáklí, A. Electrically Tunable Reflection Color of Chiral Ferroelectric Nematic Liquid Crystals *Adv Opt Mat* **2021**, *9*, 2101230.
- (19) Imrie, C. T.; Taylor, L. The preparation and properties of low molar mass liquid crystals possessing lateral alkyl chains *Liq Cryst* **1989**, *6*, 1.
- (20) Mauguin, C. Sur les cristaux liquides de M. Lehmann *Bulletin de Minéralogie* **1911**, *71*.
- (21) Robinson, C. Liquid-crystalline structures in polypeptide solutions *Tetrahedron* **1961**, *13*, 219.
- (22) Borucki, B.; Otto, H.; Meyer, T. E.; Cusanovich, M. A.; Heyn, M. P. Sensitive Circular Dichroism Marker for the Chromophore Environment of Photoactive Yellow Protein: Assignment of the 307 and 318 nm Bands to the  $n \rightarrow \pi^*$  Transition of the Carbonyl *J Phys Chem B* **2005**, *109*, 629.
- (23) Lagerwall, J. P. F.; Giesselmann, F.; Osipov, M. On the change in helix handedness at transitions between the  $SmC^*$  and phases in chiral smectic liquid crystals *Liq Cryst* **2006**, *33*, 625.
- (24) Tykarska, M.; Czerwiński, M. The inversion phenomenon of the helical twist sense in antiferroelectric liquid crystal phase from electronic and vibrational circular dichroism *Liq Cryst* **2016**, *43*, 462.
- (25) Brown, S.; Cruickshank, E.; Storey, J. M. D.; Imrie, C. T.; Pocięcha, D.; Majewska, M.; Makal, A.; Gorecka, E. Multiple Polar and Non-polar Nematic Phases *Chemphyschem* **2021**, *22*, 2506.
- (26) Pocięcha, D.; Gorecka, E.; Čepič, M.; Vaupotič, N.; Weissflog, W. Polar order and tilt in achiral smectic phases *Phys Rev E* **2006**, *74*, 021702.
- (27) Szydłowska, J.; Pocięcha, D.; Matraszek, J.; Mieczkowski, J. Mesogenic derivatives of 2S,3S-2-halogeno-3-methylpentanoic acid with helix twist inversion in the smectic  $C^*$  phase *Liq Cryst* **1999**, *26*, 1787.
- (28) Li, J.; Xia, R.; Xu, H.; Yang, J.; Zhang, X.; Kougo, J.; Lei, H.; Dai, S.; Huang, H.; Zhang, G.; Cen, F.; Jiang, Y.; Aya, S.; Huang, M.; How Far Can We Push the Rigid Oligomers/Polymers toward Ferroelectric Nematic Liquid Crystals?, *J Am Chem Soc* **2021**, *143*, 17857–17861.
- (29) Folcia, C. L.; Ortega, J.; Vidal, R.; Sierra, T.; Etxebarria, J.; The ferroelectric nematic phase: An optimum liquid crystal candidate for nonlinear optics, *Liq Cryst* **2022**, DOI: 10.1080/02678292.2022.2056927.

The ferroelectric nematic phase is a unique example of a polar phase without positional order of the constituent molecules. The properties of the ferronematic phase formed by intrinsically chiral molecules are discussed. Chirality makes the phase structure helical with the similar pitch length in the  $N^*$  and  $N_F^*$  phases, but with opposite sense. The materials show strong non-linear optical properties.



## Supporting Information

# Intrinsically chiral ferronematic liquid crystals: an inversion of the helical twist sense at the chiral nematic – chiral ferronematic phase transition

D. Pociecha,<sup>[a]</sup> R. Walker,<sup>[b]</sup> E. Cruickshank,<sup>[b]</sup> J. Szydłowska,<sup>[a]</sup> P. Rybak,<sup>[a]</sup> A. Makal,<sup>[a]</sup> J. Matraszek,<sup>[a]</sup> J. M. Wolska,<sup>[a]</sup> J.M.D. Storey,<sup>[b]</sup> and C.T. Imrie,<sup>[b]</sup> E. Gorecka\*<sup>[a]</sup>

[a] Department of Chemistry, University of Warsaw, Zwirki i Wigury 101, 02-089 Warsaw, Poland

[b] Department of Chemistry, University of Aberdeen, Old Aberdeen AB24 3UE, U.K.

### Table of contents:

- 1 Materials
- 2 Experimental methods
- 3 Crystallographic data
- 4 Additional experimental results
- 5 References

## 1. Materials

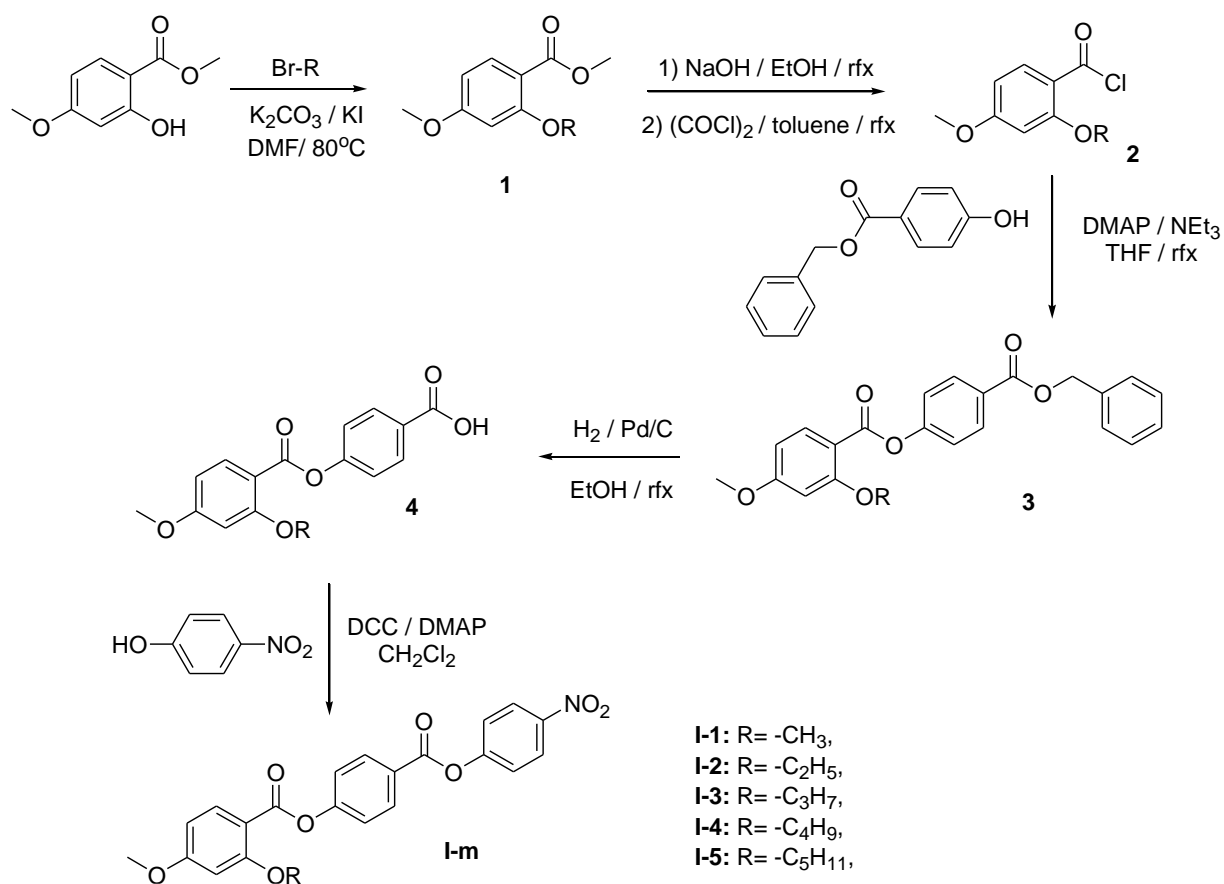
Presented reactions were carried out under an argon atmosphere using a magnetic stirring hotplate. All products were purified by column chromatography with Merck silica gel 60 (230–400 mesh). Analytical thin-layer chromatography (TLC) was performed using Merck Silica Gel 60 Å F254 pre-coated alumina plates (0.25 mm thickness) and visualized using UV lamp (254 nm) and iodine vapour. For column chromatography, the separations were carried out using silica gel grade 60 Å, 40–63 µm particle size and using an appropriate solvent system. During the synthesis following solvents of p.a. quality were used: chloroform, dichloromethane, hexane, toluene, tetrahydrofuran, ethanol and methanol. All substrates were Sigma-Aldrich or TCI products and used without further purification. Presented yields refer to chromatographically and spectroscopically (<sup>1</sup>H NMR) homogeneous materials.

### Synthesis and characterization of obtained compounds

The materials were synthesised according to previously described procedure [1] presented on Scheme 1.

Into methyl 3-hydroxy-4-methoxybenzoate the appropriate alkoxy chains were attached via the Williamson ether reaction. Next the ester group was hydrolysed and transformed into an acid chloride derivative which was substituted by the benzyl 4-hydroxybenzoate group via an esterification reaction. The protecting group was removed and 4-nitrophenol was attached via the Steglich esterification reaction to yield the target compounds. Some compounds were obtained in a slightly modified procedure outlined in Scheme 2. The ester bond in intermediate compound 3 was formed by Steglich esterification instead of using acid chloride as in pathway 1.

Following abbreviations are used:  
 DCC - N,N'-Dicyclohexylcarbodiimide  
 DMAP - 4-Dimethylaminopyridine



Scheme 1. Synthesis of the compounds series I-m

#### Analytical data of obtained materials:

The intermediate products were characterised by <sup>1</sup>HNMR spectroscopy. For the final compounds <sup>1</sup>HNMR and <sup>13</sup>CNMR spectra were recorded, and were in good agreement with the expected structures for all materials.

#### Compounds 1

##### a) Methyl 2,4-dimethoxybenzoate (R=-CH<sub>3</sub>)

<sup>1</sup>H NMR: (300MHz, CDCl<sub>3</sub>) δ: 7.83 (1H; d; J=9.0Hz); 6.49-6.44 (2H; m); 4.00 (3H; s); 3.84 (3H; s); 3.83 (3H; s); Yield: 86%

##### b) Methyl 2-ethoxy-4-methoxybenzoate (R=-C<sub>2</sub>H<sub>5</sub>)

<sup>1</sup>H NMR: (300MHz, CDCl<sub>3</sub>) δ: 7.83 (1H; d; J=9.3Hz); 6.52-6.44 (2H; m); 4.09 (2H; q; J=6.9Hz); 3.85 (3H; s); 3.83 (3H; s); 1.47 (3H; t; J=6.9Hz); Yield: 82%

##### c) Methyl 4-methoxy-2-propoxybenzoate (R=-C<sub>3</sub>H<sub>7</sub>)

<sup>1</sup>H NMR: (300MHz, CDCl<sub>3</sub>) δ: 7.84 (1H; d; J=9.0Hz); 6.52-6.43 (2H; m); 3.97 (2H; t; J=6.3Hz); 3.85 (3H; s); 3.83 (3H; s); 1.94-1.78 (2H; m); 1.08 (3H; t; J=7.5Hz); Yield: 87%



*d) Methyl 2-butoxy-4-methoxy-benzoate (R=-C<sub>4</sub>H<sub>9</sub>)*

<sup>1</sup>H NMR: (300MHz, CDCl<sub>3</sub>) δ: 7.83 (1H; d; J=9.2Hz); 6.55-6.46 (2H; m); 4.01 (2H; t; J=6.2Hz); 3.84 (3H; s); 3.83 (3H; s); 1.87-1.78 (2H; m); 1.60-1.48 (2H; m); 0.98 (3H; t; J=7.3Hz); Yield: 91%

*e) Methyl 4-methoxy-2-pentoxybenzoate (R=-C<sub>5</sub>H<sub>11</sub>)*

<sup>1</sup>H NMR: (300MHz, CDCl<sub>3</sub>) δ: 7.83 (1H; d; J=9.2Hz); 6.50-6.45 (2H; m); 4.00 (2H; t; J=6.5Hz); 3.85 (3H; s); 3.82 (3H; s); 1.91-1.82 (2H; m); 1.52-1.34 (4H; m); 0.95 (3H; t; J=7.0Hz); Yield: 90%

### **Compounds 3**

*a) 4-((Benzyloxy)carbonyl)phenyl-2,4-dimethoxybenzoate (R=-CH<sub>3</sub>)*

<sup>1</sup>H NMR: (300MHz, CDCl<sub>3</sub>) δ: 8.12 (2H; d; J=9.0Hz); 8.07 (1H; d; J=8.5Hz); 7.45-7.34 (5H; m); 7.27 (2H; d; J=9.0Hz); 6.57 (1H; dd; J=8.7Hz; J=2.2Hz); 6.51 (1H; d; J=2.2Hz); 5.37 (2H; s); 3.92 (3H; s); 3.89 (3H; s); Yield: 71%

*b) 4-((Benzyloxy)carbonyl)phenyl-2-ethoxy-4-methoxybenzoate (R=-C<sub>2</sub>H<sub>5</sub>)*

<sup>1</sup>H NMR: (300MHz, CDCl<sub>3</sub>) δ: 8.13 (2H; d; J=9.0Hz); 8.04 (1H; d; J=8.7Hz); 7.48-7.33 (5H; m); 7.28 (2H; d; J=9.0Hz); 6.55 (1H; dd; J=8.7Hz; J=2.4Hz); 6.51 (1H; d; J=2.4Hz); 5.37 (2H; s); 4.12 (2H; q; J=7.2Hz); 3.88 (3H; s); 1.47 (3H; t; J=6.9Hz); Yield: 70%

*c) 4-((Benzyloxy)carbonyl)phenyl-4-methoxy-2-propoxybenzoate (R=-C<sub>3</sub>H<sub>7</sub>)*

<sup>1</sup>H NMR: (300MHz, CDCl<sub>3</sub>) δ: 8.13 (2H; d; J=9.0Hz); 8.03 (1H; d; J=8.7Hz); 7.48-7.32 (5H; m); 7.28 (2H; d; J=9.0Hz); 6.54 (1H; dd; J=8.7Hz; J=2.4Hz); 6.51 (1H; d; J=2.4Hz); 5.37 (2H; s); 4.00 (2H; t; J=6.3Hz); 3.86 (3H; s); 1.93-1.78 (2H; m); 1.05 (3H; t; J=7.5Hz); Yield: 68%

*d) 4-((Benzyloxy)carbonyl)phenyl-2-butoxy-4-methoxybenzoate (R=-C<sub>4</sub>H<sub>9</sub>)*

<sup>1</sup>H NMR: (300MHz, CDCl<sub>3</sub>) δ: 8.13 (2H; d; J=9.2 Hz); 8.03 (1H; d; J=8.8Hz); 7.47-7.34 (5H; m); 7.25 (2H; d; J=9.1Hz); 6.56 (1H; dd; J=8.8Hz; J=2.2Hz); 6.51 (1H; d; J=2.2Hz); 5.37 (2H; s); 4.04 (2H; t; J=7.0Hz); 3.87 (3H; s); 1.87-1.77 (2H; m); 1.58-1.46 (2H; m); 0.97 (3H; t; J=7.5Hz); Yield: 60%

*e) 4-((Benzyloxy)carbonyl)phenyl-4-methoxy-2-pentoxybenzoate (R=-C<sub>5</sub>H<sub>11</sub>)*

<sup>1</sup>H NMR: (300MHz, CDCl<sub>3</sub>) δ: 8.14 (2H; d; J=9.0Hz); 8.03 (1H; d; J=8.5Hz); 7.46-7.34 (5H; m); 7.25 (2H; d; J=9.0Hz); 6.55 (1H; dd; J=8.9Hz; J=2.2Hz); 6.51 (1H; d; J=2.2Hz); 5.37 (2H; s); 4.04 (2H; t; J=7.1Hz); 3.88 (3H; s); 1.86-1.79 (2H; m); 1.52-1.23 (4H; m); 0.87 (3H; t; J=7.7Hz); Yield: 67%

### **Compounds 4**

*a) 4-(2,4-Dimethoxybenzoyloxy)benzoic acid (R=-CH<sub>3</sub>)*

<sup>1</sup>H NMR: (300MHz, acetone) δ: 8.12 (2H; d; J=8.8Hz); 8.00 (1H; d; J=8.7Hz); 7.34 (2H; d; J=8.8Hz); 6.70 (1H; dd; J=8.7Hz; J=2.2Hz); 6.64 (1H; d; J=2.2Hz); 3.93 (3H; s); 3.92 (3H; s); 1.47 (3H; t; J=6.9Hz); Yield: 61%

*b) 4-(2-Ethoxy-4-methoxybenzoyloxy)benzoic acid (R=-C<sub>2</sub>H<sub>5</sub>)*

<sup>1</sup>H NMR: (300MHz, CDCl<sub>3</sub>) δ: 8.13 (2H; d; J=8.7Hz); 8.04 (1H; d; J=8.7Hz); 7.24 (2H; d; J=8.7Hz); 6.55 (1H; dd; J=8.7Hz; J=2.4Hz); 6.51 (1H; d; J=2.4Hz); 4.12 (2H; q; J=7.8Hz); 3.87 (3H; s); 1.47 (3H; t; J=6.9Hz); Yield: 73%

c) 4-(4-Methoxy-2-propoxy-benzoyloxy)benzoic acid ( $R=-C_3H_7$ )

$^1H$  NMR: (300MHz,  $CDCl_3$ )  $\delta$ : 8.18 (2H; d;  $J=9.0$ Hz); 8.05 (1H; d;  $J=8.7$ Hz); 7.32 (2H; d;  $J=9.0$ Hz); 6.55 (1H; dd;  $J=8.7$ Hz;  $J=2.4$ Hz); 6.51 (1H; d;  $J=2.4$ Hz); 4.01 (2H; t;  $J=6.6$ Hz); 3.87 (3H; s); 1.96-1.79 (2H; m); 1.07 (3H; t;  $J=7.5$ Hz); Yield: 68%

d) 4-(2-Butoxy-4-methoxy-benzoyloxy)benzoic acid ( $R=-C_4H_9$ )

$^1H$  NMR: (300MHz,  $CDCl_3$ )  $\delta$ : 8.17 (2H; d;  $J=9.1$ Hz); 8.05 (1H; d;  $J=8.8$ Hz); 7.31 (2H; d;  $J=9.1$ Hz); 6.55 (1H; dd;  $J=8.8$ Hz;  $J=2.2$ Hz); 6.50 (1H; d;  $J=2.2$ Hz); 4.06 (2H; t;  $J=6.8$ Hz); 3.88 (3H; s); 1.86-1.79 (2H; m); 1.57-1.49 (2H; m); 0.95 (3H; t;  $J=7.5$ Hz); Yield: 75%

e) 4-(4-Methoxy-2-pentoxy-benzoyloxy)benzoic acid ( $R=-C_5H_{11}$ )

$^1H$  NMR: (300MHz,  $CDCl_3$ )  $\delta$ : 8.18 (2H; d;  $J=9.0$ Hz); 8.05 (1H; d;  $J=8.7$ Hz); 7.41 (2H; d;  $J=9.0$ Hz); 6.55 (1H; dd;  $J=8.8$ Hz;  $J=2.2$ Hz); 6.50 (1H; d;  $J=2.2$ Hz); 4.05 (2H; t;  $J=6.7$ Hz); 3.89 (3H; s); 1.88-1.83 (2H; m); 1.50-1.44 (2H; m); 1.39-1.31 (2H; m); 0.90 (3H; t;  $J=7.6$ Hz); Yield: 77%

### **Compounds I-m**

a) 4-((4-Nitrophenoxy)carbonyl)phenyl 2,4-dimethoxybenzoate ( $R=-CH_3$ ); **I-1**

$^1H$  NMR: (300MHz,  $CDCl_3$ )  $\delta$ : 8.34 (2H; d;  $J=9.2$ Hz); 8.26 (2H; d;  $J=8.7$ Hz); 8.08 (1H; d;  $J=8.7$ Hz); 7.43 (2H; d;  $J=9.1$ Hz); 7.39 (2H; d;  $J=8.8$ Hz); 6.56 (1H; dd;  $J=8.7$ Hz;  $J=2.2$ Hz); 6.51 (1H; d;  $J=2.2$ Hz); 4.07 (2H; t;  $J=6.9$ Hz); 3.89 (3H; s);

$^{13}C$  NMR (75MHz,  $CDCl_3$ )  $\delta$ : 165.54; 163.86; 163.20; 162.35; 156.21; 156.00; 145.57; 134.89; 132.05; 125.72; 125.43; 122.89; 122.63; 110.49; 105.17; 99.89; 64.99; 56.20; 55.73; Yield: 45%

b) 4-((4-Nitrophenoxy)carbonyl)phenyl 2-ethoxy-4-methoxybenzoate ( $R=-C_2H_5$ ); **I-2**

$^1H$  NMR: (300MHz,  $CDCl_3$ )  $\delta$ : 8.33 (2H; d;  $J=9.3$ Hz); 8.26 (2H; d;  $J=8.7$ Hz); 8.08 (1H; d;  $J=8.7$ Hz); 7.43 (2H; d;  $J=9.3$ Hz); 7.39 (2H; d;  $J=8.7$ Hz); 6.57 (1H; dd;  $J=8.7$ Hz;  $J=2.4$ Hz); 6.51 (1H; d;  $J=2.4$ Hz); 4.14 (2H; q;  $J=6.9$ Hz); 3.89 (3H; s); 1.49 (3H; t;  $J=6.9$ Hz);

$^{13}C$  NMR (75MHz,  $CDCl_3$ )  $\delta$ : 165.58; 163.96; 163.37; 162.19; 156.41; 156.04; 145.77; 134.89; 132.25; 125.86; 125.63; 122.99; 122.83; 111.00; 105.37; 100.23; 64.99; 55.93; 15.00; Yield: 50%

c) 4-((4-Nitrophenoxy)carbonyl)phenyl 4-methoxy-2-propoxybenzoate ( $R=-C_3H_7$ ); **I-3**

$^1H$  NMR: (300MHz,  $CDCl_3$ )  $\delta$ : 8.33 (2H; d;  $J=9.3$  Hz); 8.26 (2H; d;  $J=9.0$  Hz); 8.06 (1H; d;  $J=8.7$ Hz); 7.42 (2H; d;  $J=9.3$ Hz); 7.39 (2H; d;  $J=9.0$ Hz); 6.56 (1H; dd;  $J=8.7$ Hz;  $J=2.4$ Hz); 6.51 (1H; d;  $J=2.4$ Hz); 4.03 (2H; t;  $J=6.3$ Hz); 3.89 (3H; s); 1.96-1.81 (2H; m); 1.07 (3H; t;  $J=7.5$ Hz);

$^{13}C$  NMR (75MHz,  $CDCl_3$ )  $\delta$ : 165.59; 163.97; 163.56; 162.28; 156.45; 156.05; 145.77; 134.98; 132.29; 125.86; 125.64; 123.00; 122.83; 111.99; 105.33; 100.05; 70.77; 55.94; 22.86; 10.96; Yield: 48%

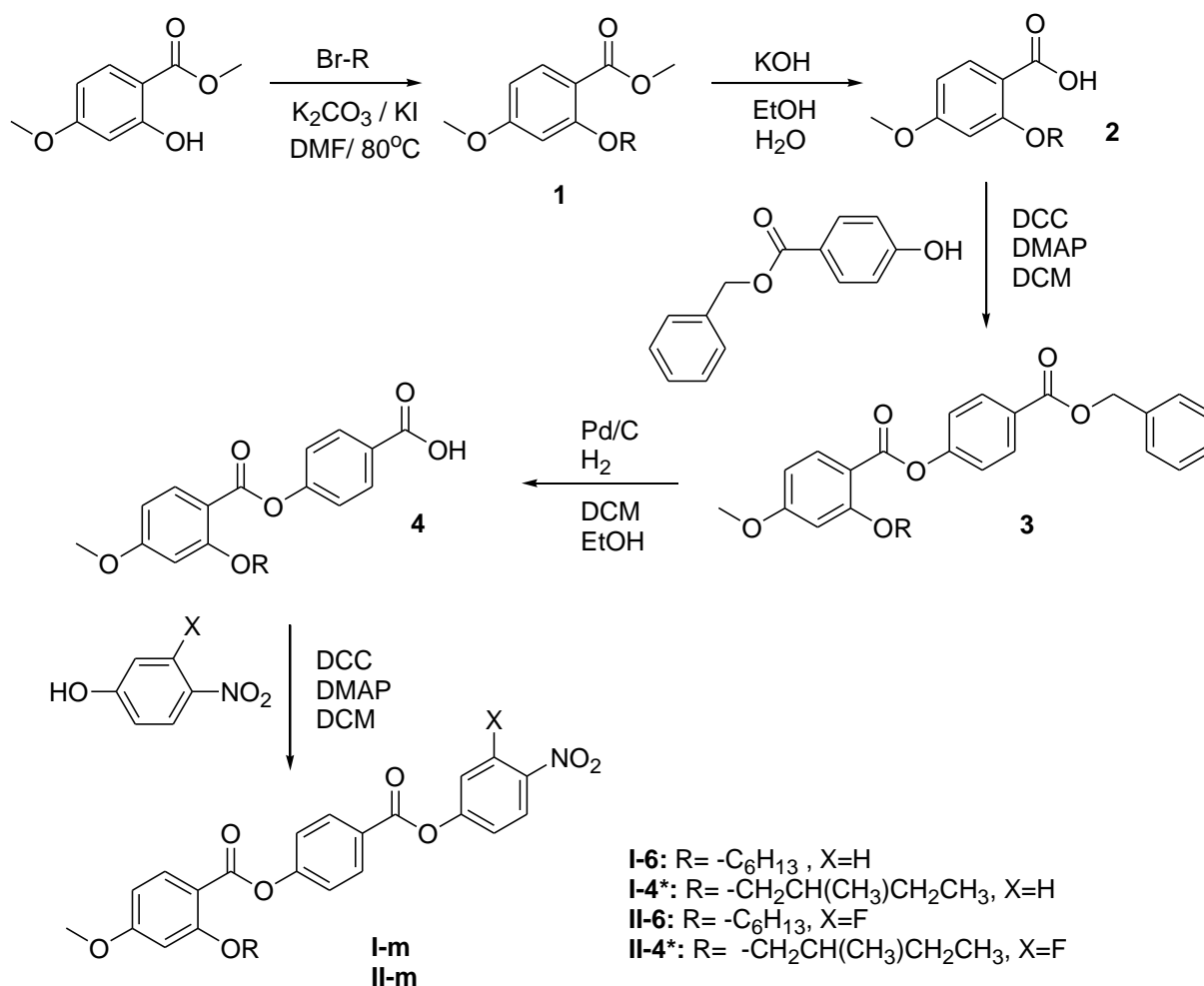
d) 4-((4-Nitrophenoxy)carbonyl)phenyl 2-butoxy-4-methoxybenzoate ( $R=-C_4H_9$ ); **I-4**

$^1H$  NMR: (300MHz,  $CDCl_3$ )  $\delta$ : 8.33 (2H; d;  $J=9.1$ Hz); 8.25 (2H; d;  $J=9.0$  Hz); 8.06 (1H; d;  $J=8.8$ Hz); 7.43 (2H; d;  $J=9.0$ Hz); 7.37 (2H; d;  $J=9.0$ Hz); 6.56 (1H; dd;  $J=8.8$ ;  $J=2.2$  Hz); 6.51 (1H; d;  $J=2.2$ Hz); 4.03 (2H; t;  $J=6.5$ Hz); 3.90 (3H; s); 1.94-1.84 (2H; m); 1.60-1.48 (2H; m); 1.00 (3H; t;  $J=7.6$ Hz);

$^{13}C$  NMR (75MHz,  $CDCl_3$ )  $\delta$ : 165.61; 163.91; 163.45; 162.62; 156.19; 156.04; 145.82; 134.79; 131.95; 125.91; 125.63; 122.75; 122.55; 112.02; 105.55; 99.73; 68.57; 56.21; 31.20; 19.31; 14.00; Yield: 43%

e) 4-((4-Nitrophenoxy)carbonyl)phenyl 4-methoxy-2-pentoxybenzoate ( $R=C_5H_{11}$ ); **I-5**

$^1H$  NMR: (300MHz,  $CDCl_3$ )  $\delta$ : 8.34 (2H; d;  $J=9.1$ Hz); 8.26 (2H; d;  $J=9.1$ Hz); 8.06 (1H; d;  $J=8.7$ Hz); 7.43 (2H; d;  $J=9.1$ Hz); 7.38 (2H; d;  $J=9.1$ Hz); 6.56 (1H; dd;  $J=8.7$ Hz;  $J=2.2$ Hz); 6.52 (1H; d;  $J=2.2$ Hz); 4.06 (2H; t;  $J=6.7$ Hz); 3.90 (3H; s); 1.92-1.82 (2H; m); 1.51-1.46 (2H; m); 1.40-1.34 (2H; m); 0.90 (3H; t;  $J=7.5$ Hz);  $^{13}C$  NMR (75MHz,  $CDCl_3$ )  $\delta$ : 165.60; 163.90; 163.48; 162.22; 156.40; 156.04; 145.78; 134.90; 131.95; 125.86; 125.63; 122.68; 122.50; 111.99; 105.35; 99.73; 68.97; 55.61; 28.81; 28.14; 22.39; 14.00; Yield: 47%



Scheme 2. Synthesis of the compounds series **I-m** and **II-m**

**Compound 1**

a) 2-Hexyloxy-4-methoxy-benzoic acid methyl ester

$^1H$  NMR (400 MHz,  $CDCl_3$ )  $\delta$  ppm: 7.85 (d,  $J = 8.5$  Hz, 1H), 6.52 – 6.44 (m, 2H), 4.01 (t,  $J = 6.5$  Hz, 2H), 3.85 (m, 6H), 1.85 (m, 2H), 1.54 – 1.46 (m, 2H), 1.36 (m, 4H), 0.92 (m, 3H). Yield: 75.5 %

b) (S)-4-Methoxy-2-(2-methyl-butoxy)-benzoic acid methyl ester

$^1H$  NMR (400 MHz,  $CDCl_3$ )  $\delta$  ppm: 7.86 (d,  $J = 8.6$  Hz, 1H), 6.52 – 6.42 (m, 2H), 3.94 – 3.81 (m, 8H), 1.92 (m, 1H), 1.70 – 1.55 (m, 1H), 1.41 – 1.20 (m, 1H), 1.08 (d,  $J = 6.7$  Hz, 3H), 0.97 (t,  $J = 7.4$  Hz, 3H). Yield: 30.1 %

## **Compound 2**

### *a) 2-Hexyloxy-4-methoxy-benzoic acid*

$^1\text{H}$  NMR (400 MHz, DMSO)  $\delta$  ppm: 7.46 (d,  $J$  = 8.6 Hz, 1H), 6.41 – 6.29 (m, 2H), 3.79 (t,  $J$  = 6.4 Hz), 3.58 (s, 3H), 1.54 – 1.42 (m, 2H), 1.22 (p,  $J$  = 7.2 Hz, 2H), 1.08 (m, 4H), 0.65 (m, 3H). Yield: 90.1 %

### *b) (S)-4-Methoxy-2-(2-methyl-butoxy)-benzoic acid*

$^1\text{H}$  NMR (400 MHz, DMSO)  $\delta$  ppm: 7.68 (d,  $J$  = 8.6 Hz, 1H), 6.70 – 6.43 (m, 2H), 3.94 – 3.77 (m, 5H), 1.87 – 1.75 (m,  $J$  = 6.5 Hz, 1H), 1.55 (m, 1H), 1.25 (m, 1H), 0.99 (d,  $J$  = 6.7 Hz, 3H), 0.90 (t,  $J$  = 7.4 Hz, 3H). Yield: 98.1 %

## **Compound 3**

### *a) 2-Hexyloxy-4-methoxy-benzoic acid 4-benzyloxycarbonyl-phenyl ester*

$^1\text{H}$  NMR (400 MHz,  $\text{CDCl}_3$ )  $\delta$  ppm: 8.24 – 8.11 (m, 2H), 8.05 (d,  $J$  = 8.8 Hz, 1H), 7.55 – 7.21 (m, 7H), 6.62 – 6.47 (m, 2H), 5.40 (s, 2H), 4.06 (t,  $J$  = 6.5 Hz, 2H), 3.90 (s, 3H), 1.91 – 1.80 (m, 2H), 1.55 – 1.44 (m, 2H), 1.40 – 1.18 (m, 4H), 0.93 – 0.84 (m, 3H). Yield: 73.8 %

### *b) (S)-4-Methoxy-2-(2-methyl-butoxy)-benzoic acid 4-benzyloxycarbonyl-phenyl ester*

$^1\text{H}$  NMR (400 MHz, DMSO)  $\delta$  ppm: 8.08 (d,  $J$  = 8.6 Hz, 2H), 7.94 (d,  $J$  = 8.7 Hz, 1H), 7.54 – 7.28 (m, 7H), 6.74 – 6.58 (m, 2H), 5.37 (s, 2H), 3.98 – 3.88 (m, 2H), 3.87 (s, 3H), 1.80 (m, 1H), 1.61 – 1.46 (m, 1H), 1.32 – 1.19 (m, 1H), 0.97 (d,  $J$  = 6.7 Hz, 3H), 0.86 (t,  $J$  = 7.5 Hz, 3H). Yield: 67.7 %

## **Compound 4**

### *a) 2-Hexyloxy-4-methoxy-benzoic acid 4-carboxy-phenyl ester*

$^1\text{H}$  NMR (400 MHz, DMSO)  $\delta$  ppm: 13.01 (s, 1H), 8.06 – 7.98 (m, 2H), 7.92 (d,  $J$  = 8.7 Hz, 1H), 7.36 – 7.29 (m, 2H), 6.72 – 6.63 (m, 2H), 4.08 (t,  $J$  = 6.2 Hz, 2H), 3.87 (s, 3H), 1.72 (p,  $J$  = 6.6 Hz, 2H), 1.43 (q,  $J$  = 7.5 Hz, 2H), 1.24 (m, 4H), 0.80 (t,  $J$  = 6.9 Hz, 3H). Yield: 92.7 %

### *b) (S)-4-Methoxy-2-(2-methyl-butoxy)-benzoic acid 4-carboxy-phenyl ester*

$^1\text{H}$  NMR (400 MHz, DMSO)  $\delta$  ppm: 13.01 (s, 1H), 8.06 – 7.98 (m, 2H), 7.93 (d,  $J$  = 8.7 Hz, 1H), 7.36 – 7.29 (m, 2H), 6.72 – 6.63 (m, 2H), 3.96 (m, 2H), 3.87 (s, 3H), 1.81 (h,  $J$  = 6.4 Hz, 1H), 1.61 – 1.49 (m, 1H), 1.24 (m, 1H), 0.98 (d,  $J$  = 6.7 Hz, 3H), 0.87 (t,  $J$  = 7.4 Hz, 3H). Yield: 56.3 %

## **Compound I-m**

### *a) 2-Hexyloxy-4-methoxy-benzoic acid 4-(4-nitro-phenoxy-carbonyl)-phenyl ester, I-6*

$^1\text{H}$  NMR (400 MHz, DMSO)  $\delta$  ppm: 8.38 (d,  $J$  = 8.9 Hz, 2H), 8.25 (d,  $J$  = 8.3 Hz, 2H), 7.95 (d,  $J$  = 8.7 Hz, 1H), 7.66 (d,  $J$  = 8.7 Hz, 2H), 7.47 (d,  $J$  = 8.3 Hz, 2H), 6.71 – 6.64 (m, 2H), 4.10 (t,  $J$  = 6.2 Hz, 2H), 3.88 (s, 3H), 1.73 (p,  $J$  = 6.8 Hz, 2H), 1.45 (p,  $J$  = 7.3 Hz, 2H), 1.25 (m, 4H), 0.82 (t,  $J$  = 6.8 Hz, 3H).  $^{13}\text{C}$  NMR (101 MHz, DMSO)  $\delta$  ppm: 165.42, 163.79, 163.29, 161.68, 156.02, 155.97, 145.69, 134.52, 132.22, 126.03, 125.81, 123.86, 123.16, 110.40, 106.34, 100.08, 68.85, 56.20, 31.35, 29.00, 25.59, 22.51, 14.31. Yield: 14.4 %

### *b) (S)-4-Methoxy-2-(2-methyl-butoxy)-benzoic acid 4-(4-nitro-phenoxy-carbonyl)-phenyl ester, I-4\**

$^1\text{H}$  NMR (400 MHz, DMSO)  $\delta$  ppm: 8.43 – 8.32 (m, 2H), 8.29 – 8.22 (m, 2H), 7.96 (d,  $J$  = 8.7 Hz, 1H), 7.69 – 7.62 (m, 2H), 7.47 (d,  $J$  = 8.6 Hz, 2H), 6.74 – 6.64 (m, 2H), 3.98 (m, 2H), 3.88 (s, 3H), 1.83 (h,  $J$  = 6.4 Hz, 1H), 1.63 – 1.48 (m, 1H), 1.26 (m, 1H), 0.99 (d,  $J$  = 6.7 Hz, 3H), 0.88 (t,  $J$  = 7.4 Hz, 3H).  $^{13}\text{C}$  NMR

(100 MHz, DMSO)  $\delta$  ppm: 165.47, 163.75, 163.31, 161.81, 156.01, 155.97, 145.65, 134.58, 132.24, 126.03, 125.78, 123.84, 123.15, 110.19, 106.34, 99.86, 73.29, 56.20, 34.70, 25.86, 16.79, 11.65. m/z: [M+H]<sup>+</sup> Calculated mass for C<sub>26</sub>H<sub>26</sub>NO<sub>8</sub>: 480.1658, Found: 480.1653. Difference: 1.0 ppm. Yield: 39.8 %

#### **Compound II-m**

a) 2-Hexyloxy-4-methoxy-benzoic acid 4-(3-fluoro-4-nitro-phenoxy-carbonyl)-phenyl ester, **II-6**

<sup>1</sup>H NMR (400 MHz, DMSO)  $\delta$  ppm: 8.33 (t, *J* = 8.9 Hz, 1H), 8.24 (d, *J* = 8.6 Hz, 2H), 7.96 (d, *J* = 8.7 Hz, 1H), 7.80 (m, 1H), 7.49 (m, 3H), 6.86 – 6.35 (m, 2H), 4.10 (t, *J* = 6.2 Hz, 2H), 3.88 (s, 3H), 1.73 (p, *J* = 6.6 Hz, 2H), 1.44 (m, 2H), 1.29 – 1.19 (m, 4H), 0.82 (t, *J* = 6.8 Hz, 3H);

<sup>19</sup>F NMR (376 MHz, DMSO)  $\delta$  ppm: -115.37;

<sup>13</sup>C NMR (100 MHz, DMSO)  $\delta$  ppm: 165.41, 163.44, 163.24, 161.67, 156.99, 156.10, 155.98, 154.38, 135.24, 135.17, 134.51, 132.28, 128.00, 125.76, 123.18, 119.72, 119.68, 113.43, 113.19, 110.35, 106.33, 100.07, 68.84, 56.20, 31.35, 29.00, 25.59, 22.51, 14.31. Yield: 11.5 %

b) (*S*)-4-Methoxy-2-(2-methyl-butoxy)-benzoic acid 4-(3-fluoro-4-nitro-phenoxy-carbonyl)-phenyl ester, **II-4\***

<sup>1</sup>H NMR (400 MHz, DMSO)  $\delta$  ppm: 8.33 (t, *J* = 8.8 Hz, 1H), 8.28 – 8.21 (m, 2H), 7.96 (d, *J* = 8.7 Hz, 1H), 7.79 (m, 1H), 7.49 (t, *J* = 9.3 Hz, 3H), 6.76 – 6.59 (m, 2H), 4.04 – 3.91 (m, 2H), 3.88 (s, 3H), 1.83 (q, *J* = 6.5 Hz, 1H), 1.56 (m, 1H), 1.26 (m, 1H), 0.99 (d, *J* = 6.7 Hz, 3H), 0.88 (t, *J* = 7.4 Hz, 3H);

<sup>19</sup>F NMR (376 MHz, DMSO)  $\delta$  ppm: -115.38.

<sup>13</sup>C NMR (100 MHz, DMSO)  $\delta$  ppm: 165.49, 163.44, 163.31, 161.81, 156.99, 156.10, 156.00, 154.38, 134.59, 135.25, 135.18, 132.32, 128.01, 125.78, 123.19, 119.73, 119.69, 113.44, 113.20, 110.17, 106.37, 99.87, 73.29, 56.22, 34.69, 25.86, 16.80, 11.66. Yield: 8.7 %

## 2. Experimental methods

**NMR spectra:** NMR spectra were recorded on a NMR Bruker AVANCE 300 MHz spectrometer (for compounds showed in the Scheme 1) or a NMR Bruker Avance III HD 400 MHz spectrometer (for compounds showed in Scheme 2) using tetramethylsilane as an internal standard. Chemical shifts are reported in ppm.

**Calorimetric Measurements:** Calorimetric studies were performed with a TA DSC Q200 calorimeter, 1 - 3 mg samples were sealed in aluminum pans and kept in a nitrogen atmosphere during measurement, and both heating and cooling scans were performed with a rate of 5–10 K/min.

**Microscopic Studies:** Optical studies were performed by using the Zeiss Axio Imager A2m polarized light microscope, equipped with Linkam heating stage. Samples were prepared in commercial cells (AWAT) of various thickness (1.5 – 20  $\mu\text{m}$ ) having ITO electrodes and surfactant layer for either planar or homeotropic alignment, HG and HT cells, respectively.

**X-Ray Diffraction:** The wide angle X-ray diffraction patterns were obtained with the Bruker D8 GADDS system (CuK $\alpha$  radiation, Goebel mirror monochromator, 0.5 mm point beam collimator, Vantec2000 area detector), equipped with modified Linkam heating stage. Samples were prepared as droplets on a heated surface. For single crystal X-ray diffraction measurements a sample was mounted on a kapton loop with a drop of ParatoneN oil. Intensity data were measured on Rigaku Oxford Diffraction Supernova 4 circle diffractometer equipped with copper (CuK $\alpha$ ) microsource and Atlas CCD detector at 120K. The temperature of the sample was controlled with a precision of  $\pm 0.1$  K using Oxford Cryosystems cooling device. The data were collected, integrated and scaled with CrysAlis1711 software [2]. The structures were solved by direct methods using SHELXT [3] and refined by full-matrix least squares procedure with SHELXL [4] within OLEX2 [5] graphical interface. Structures were deposited with CCDC (2130530 for **I-3** and 2130531 for **I-4**) and can be retrieved upon request.

**Birefringence Measurements:** Birefringence was measured with a setup based on a photoelastic modulator (PEM-90, Hinds) working at a modulation frequency  $f = 50$  kHz; as a light source, a halogen lamp (Hamamatsu LC8) was used, equipped with a narrow bandpass filter (532 nm). The signal from a photodiode (FLC Electronics PIN-20) was de-convoluted with a lock-in amplifier (EG&G 7265) into 1f and 2f components to yield a retardation induced by the sample. Knowing the sample thickness, the retardation was recalculated into optical birefringence. Uniformly aligned samples in HG cells, 1.5- and 3- $\mu\text{m}$ -thick, were measured.

**Optical Rotatory Power, circular dichroism (CD) and selective reflection measurements:** ORP was measured using Nikon OPTIPHOT2-POL microscope equipped with rotating polarizer mounted below the sample and analyzer at fixed position above the sample. The intensity of light transmitted through the optical setup was measured by photomultiplier mounted on the microscope. The light intensity as a function of lower polarizer position, in the range 0-180 deg., was fitted to the sinusoidal function to find the extinction position. ORP was measured for samples of various thickness (3-10  $\mu\text{m}$ ) prepared using either glasses treated with polymer to induce planar alignment of molecules or CaF<sub>2</sub> crystal plates with no polymer layer.

Selective reflection was measured using  $\sim 10$ -15  $\mu\text{m}$  thick cells made of CaF<sub>2</sub> crystal plates, placed in the Linkam hot stage, FTIR spectra in the range 10000-3500  $\text{cm}^{-1}$  (in this range no molecular bands are observed) were collected with Thermo Scientific Nicolet 6700FT-IR spectrometer. Circular dichroism (CD) spectra in the wavelength range 200-600 nm were recorded using Applied Photophysics Chirascan Plus instrument, the temperature of the sample was controlled by Peltier heater, the sample was placed between quartz plates.

Absorption spectra were measured for methylene chloride solutions using Shimadzu PC3100 spectrometer.

**Spontaneous Electric Polarization Measurements:** Values of the spontaneous electric polarization were obtained from the current peaks recorded during Ps switching upon applying triangular voltage at a frequency of 2 Hz. The 5- $\mu\text{m}$ -thick cells with ITO electrodes and no polymer aligning layers were used, switching current was determined by recording the voltage drop at the resistivity of 50 kOhm in serial connection with the sample. The current peak was integrated over time to calculate the surface electric charge and evaluate polarization value. It was checked that under such conditions the saturated values of polarization were obtained, and thus it was not necessary to use in-plane switching method, proposed in previous reports [1, 6, 7].

**Dielectric spectroscopy:** The complex dielectric permittivity,  $\epsilon^*$ , was studied using Solatron 1260 impedance analyzer, measurements were conducted in 1 Hz – 10 MHz frequency ( $f$ ) range, with the probe voltage 20 mV, and it was checked by optical observations that such a voltage is below Fredericks transition. Material was placed in glass cells with ITO or Au electrodes and thickness ranging from 5 to 10 microns. Cells without polymer aligning layers were used, as presence of the thin ( $\sim 10$  nm) polyimide layers at the cell surfaces acts as additional high capacitance being in series circuit with the capacitor filled with LC sample, and for studied here materials with very high permittivity this may strongly disturb measured permittivity of LC phases. Lack of surfactant layer resulted in random configuration of director in LC phases, microscopic observations of optical textures suggested dominant planar orientation without preferable direction of long molecular axis.

The relaxation frequency,  $f_r$ , and dielectric strength of the mode,  $\Delta\epsilon$ , were evaluated by fitting complex dielectric permittivity to the Cole-Cole formula:  $\epsilon - \epsilon_\infty = \sum \frac{\Delta\epsilon}{(1 + \frac{if}{f_r})^{1-\alpha}} + i \frac{\delta}{2\pi\epsilon_0 f}$ , where  $\epsilon_\infty$  is high frequency dielectric constant,  $\alpha$  is distribution parameter of the mode and  $\sigma$  is low frequency conductivity, respectively.

**SHG measurements:** The SHG response was investigated using solid-state laser EKSPLA NL202. The 9 ns laser pulses at 10 Hz repetition rate and maximal  $\sim 2$  mJ power in the pulse at  $\lambda=1064$  nm were applied. Pulse energy was adjusted to each sample to avoid its decomposition. The infra-red beam was incident onto the LC homogenous cell of thickness 1.7-20  $\mu\text{m}$ . IR pass filter was placed at the entrance to the sample and green pass filter at exit of the sample, the emitted SHG radiation was detected using photon counting head (Hamamatsu H7421) with power supply unit (C8137). The signal intensity was estimated by photon counting software connected to the oscilloscope (Agilent Technologies DSO6034A). For some experiments a bias electric field (up to 3 V  $\mu\text{m}^{-1}$ ) was applied, perpendicular to the sample surface, thus along the incident beam.

### 3. Crystallographic data

#### 3.1 Compound I-4

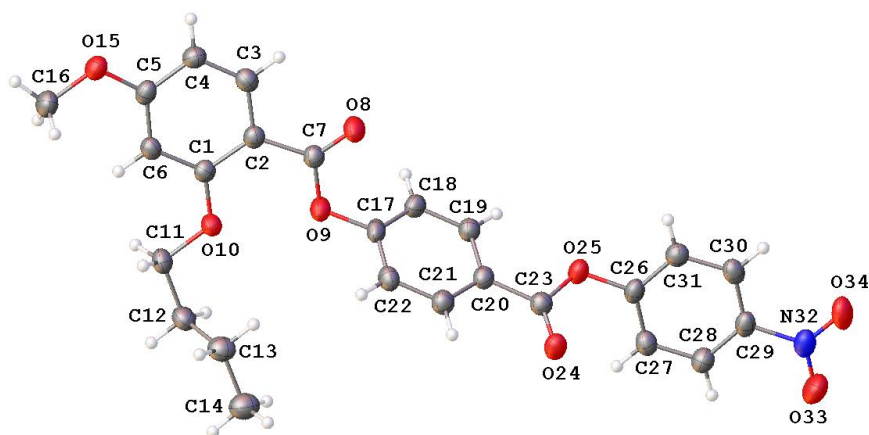


**Figure S1.** Molecular structure of compound **I-4** determined from crystal data and structure refinement, representation with atomic displacement parameters at 50% probability level.

#### Crystal data and structure refinement for compound I-4

Crystal system: monoclinic  
Space group:  $P2_1/c$   
Formula:  $C_{25}H_{23}NO_8$

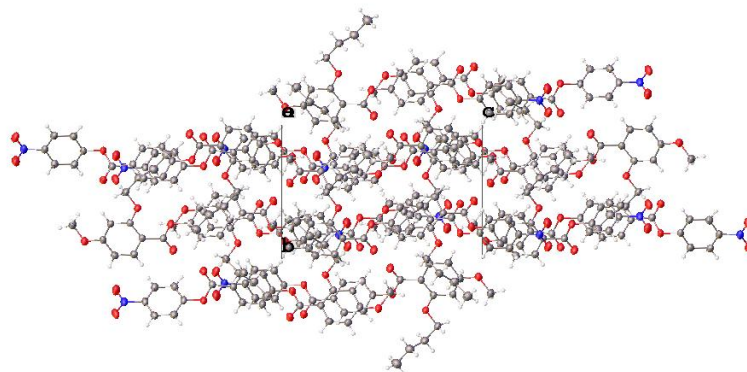
$a = 16.6955(16) \text{ \AA}$   
 $b = 9.3735(7) \text{ \AA}$   
 $c = 15.0994(12) \text{ \AA}$   
 $\alpha = 90^\circ$   
 $\beta = 111.798(9)^\circ$   
 $\gamma = 90^\circ$   
 $V = 2194.0(3) \text{ \AA}^3$   
 $Z = 4$

There is 1 molecule in the asymmetric unit and 4 molecules in the unit cell, and no traces of solvent in the structure. The molecule displays a single conformation with the lateral aliphatic chain in fully stretched conformation, there is no traces of disorder. The angles between the planes of the consecutive phenyl rings (ring I: C1 – C6, ring II: C18 – C22, ring III: C26 - C30), are about 60 degrees. The molecules are aligned along [2,0,1] crystallographic direction. The molecules related by  $C_{[010]}$  glide plane display  $\pi \dots \pi$  stacking of the phenyl rings I with II and II with III. Other intermolecular interactions involve: C – H ... O interactions from methoxy group and the aliphatic linker  $CH_2$  towards the carbonyl oxygens O8 and O24 C – H ... O interactions from phenyl group III towards the oxygens of the nitro group.

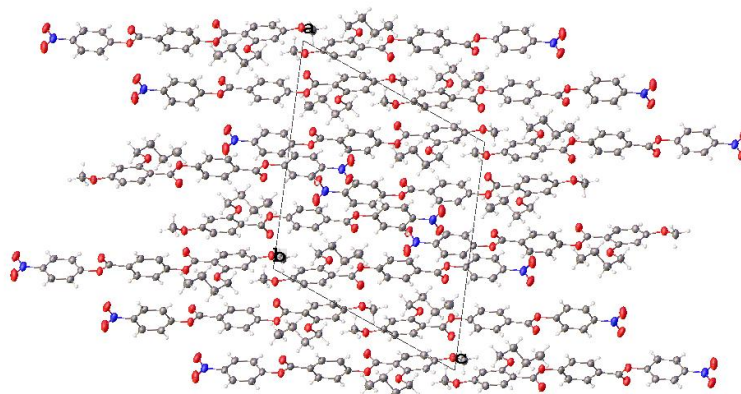
The molecules of **I-4** do not form clearly separated layers in the crystal structure.



[100]



[010]



[001]

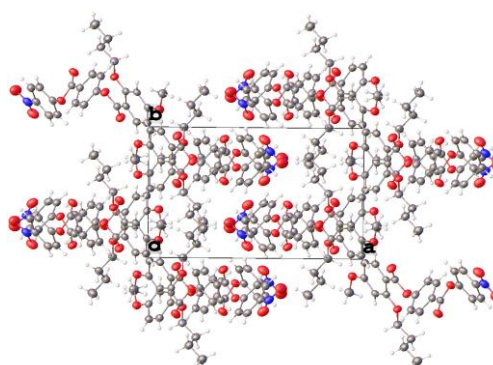


**Figure S2.** Orientation of molecules **I-4** in crystal lattice viewed along [100], [010] and [001] crystallographic directions.

### 3.2 Compound I-3

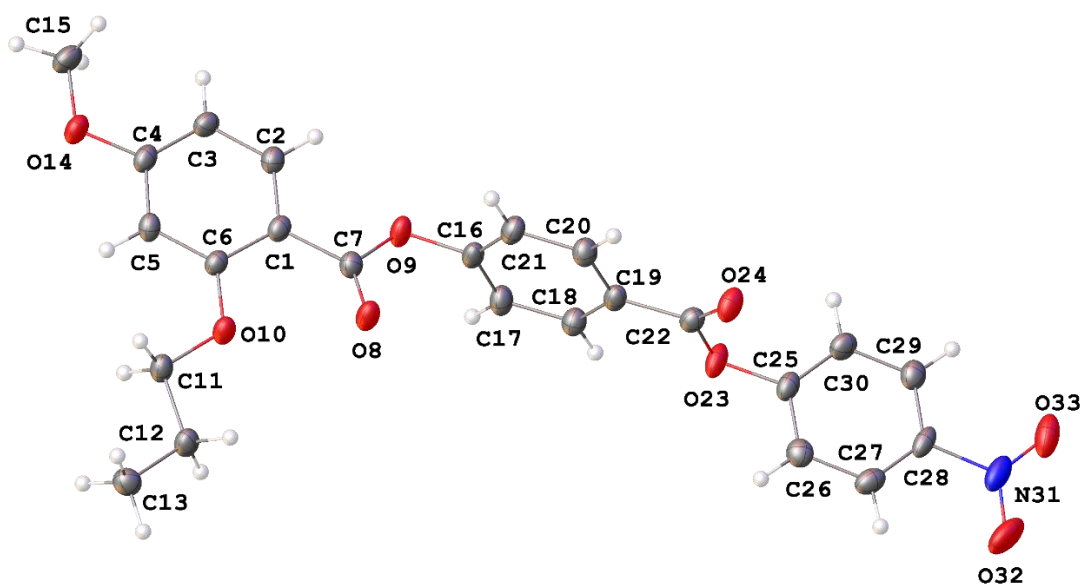


**Figure S3.** Molecular structure of compound **I-3** determined from crystal data and structure refinement, representation with atomic displacement parameters at 50% probability level.

#### Crystal data and structure refinement for compound I-3

Crystal system: monoclinic  
Space group:  $P2_1/c$   
Formula:  $C_{24}H_{21}NO_8$

$a = 11.0413(7) \text{ \AA}$   
 $b = 25.266(2) \text{ \AA}$   
 $c = 7.7947(7) \text{ \AA}$   
 $\alpha = 90^\circ$   
 $\beta = 103.501(7)^\circ$   
 $\gamma = 90^\circ$   
 $V = 2144.4(3) \text{ \AA}^3$   
 $Z = 4$

Compound crystallizes in monoclinic system in centrosymmetric space group, with one molecule constituting the asymmetric unit and no solvent. Three aromatic rings are not exactly co-planar, but adopt similar tilt. Major intermolecular interaction is  $\pi$ -stacking of the flat nitrophenyl rings of two antiparallel molecules, as illustrated in Figure S4.

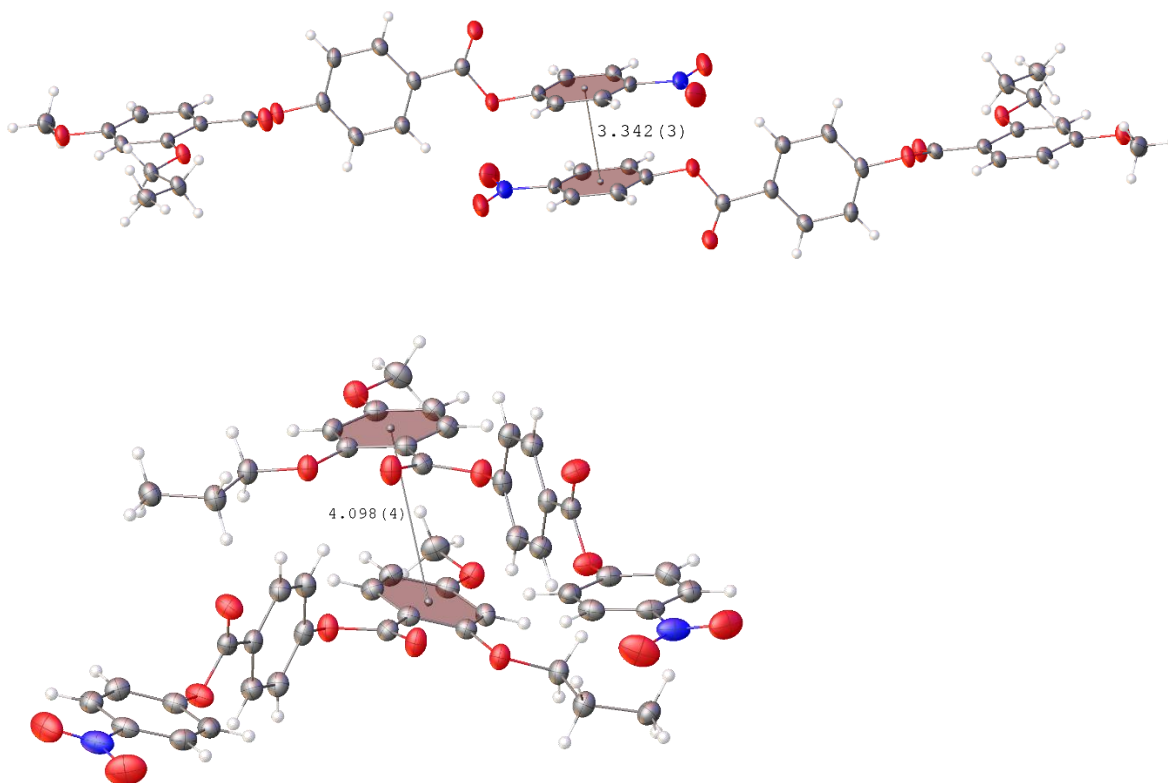


**Figure S4.** The most important intermolecular interactions in crystal structure of compound I-3.

## 4. Additional experimental results

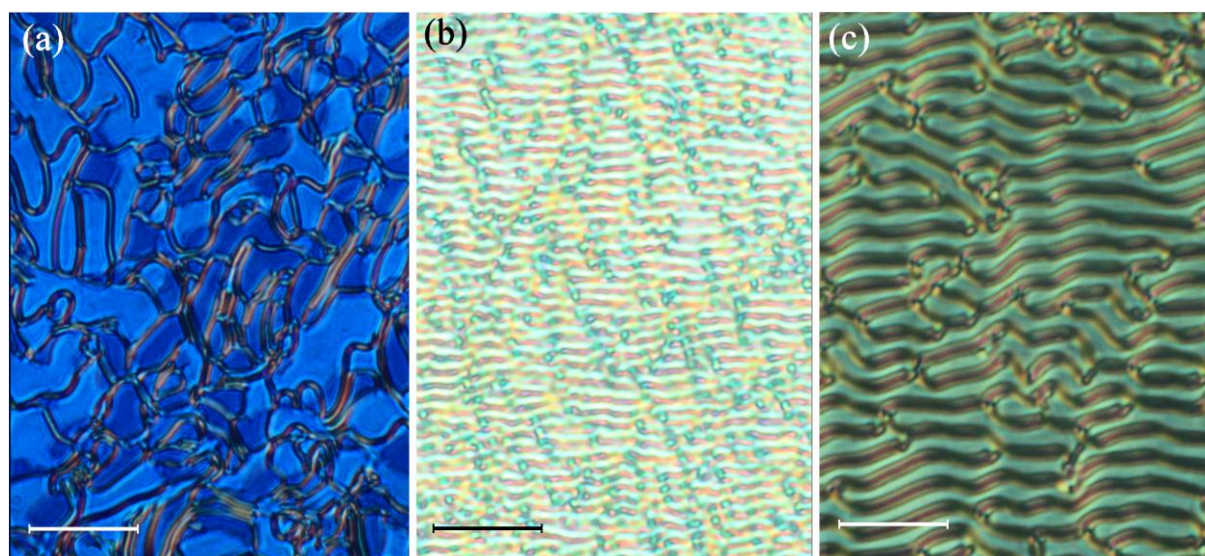


**Figure S5.** Optical textures (crossed polarizers) of  $N^*_F$  phase for compounds: (a) **I-4\***, fast cooled sample, (b) **I-4\***, slow cooled sample and (c) **II-4\***, slowly cooled sample, all images were taken at room temperature in a 5- $\mu\text{m}$ -thick cells with planar anchoring condition. Scale bars correspond to 20 microns.

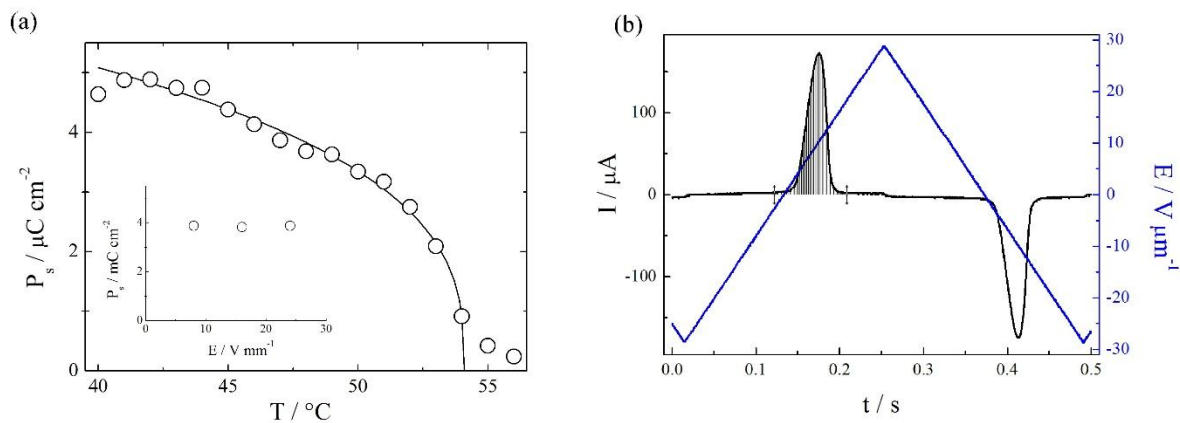


**Figure S6.** (a) Spontaneous electric polarization of  $N^*_F$  phase vs. temperature for compound: **I-4\***, in the inset polarization vs. applied electric field, measured at  $T = 47^\circ\text{C}$ ; (b) switching current (black line) associated with polarization reversal under applied triangular voltage (blue line), indicated area correspond to measured surface charge. Measurements were performed in 5- $\mu\text{m}$ -thick cell with ITO electrodes and no polymer aligning layers.

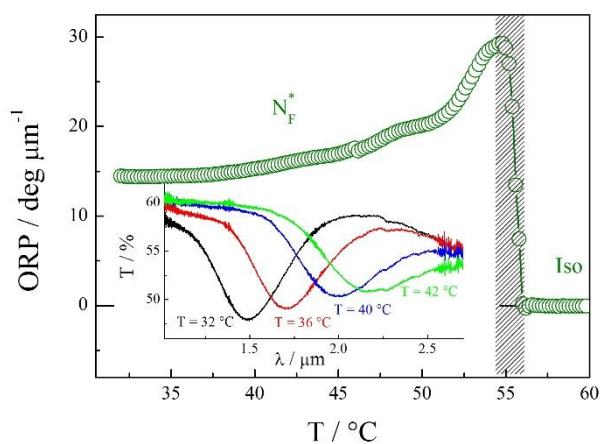


**Figure S7.** ORP vs. temperature for compound II-4\*. In the inset, the dependence of transmittance vs. wavelength at chosen temperatures in  $N_F^*$  phase range, showing selective reflection band (corresponding to half pitch).

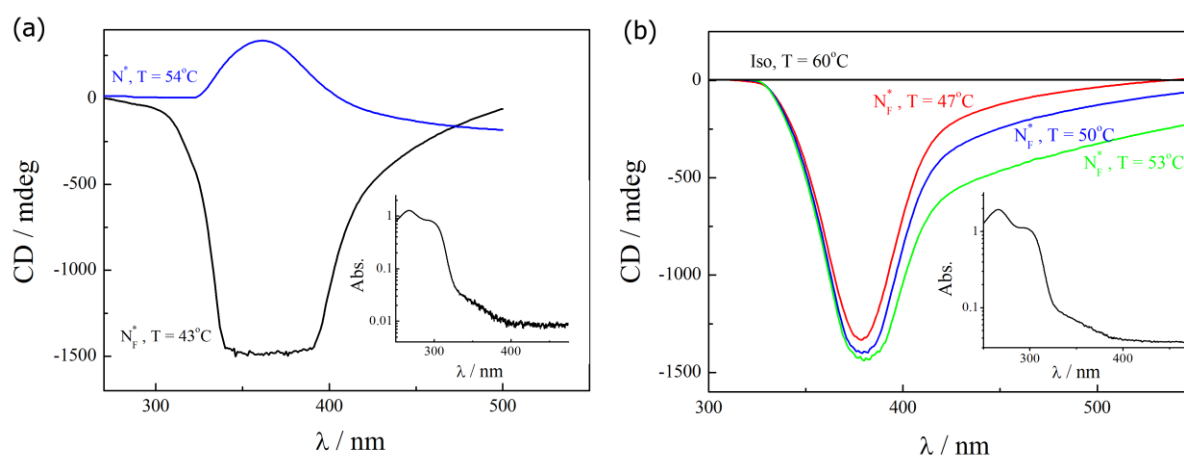


**Figure S8.** CD signal for: (a) compound I-4\* in  $N^*$  and  $N_F^*$  phases (note that signal in  $N_F^*$  phase is saturated) and (b) compound II-4\* in isotropic and  $N_F^*$  phases. In the insets: absorption spectra taken in DCM solution.

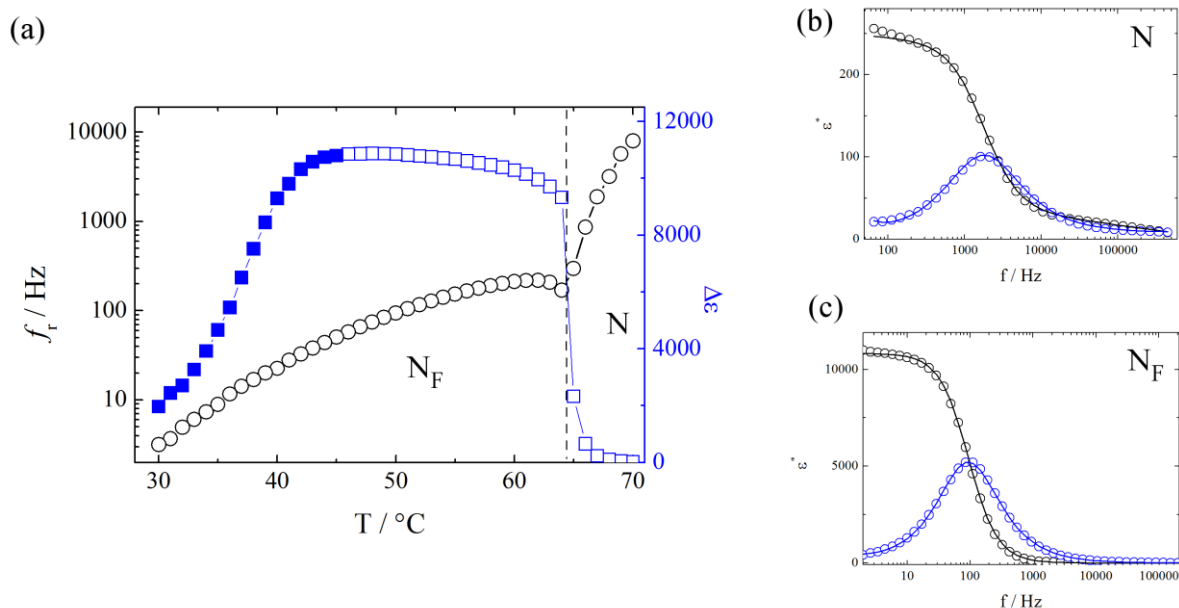


**Figure S9.** (a) Temperature dependence of relaxation frequency,  $f_r$  (black) and dielectric strength,  $\Delta\epsilon$  of the mode (blue) for compound **I-4** in 10- $\mu\text{m}$ -thick cell with ITO electrodes and no aligning layers. Note that full symbols do not represent actual  $\Delta\epsilon$  values due to partial recrystallization of the sample. (b) and (c) Examples of the fitting of the complex dielectric permittivity dispersion to Cole-Cole formula, in  $N$  ( $T = 67$  °C) and  $N_F$  ( $T = 50$  °C) phases. Circles are measured, real (black) and imaginary (blue) parts of dielectric permittivity, lines represent fitted curves.

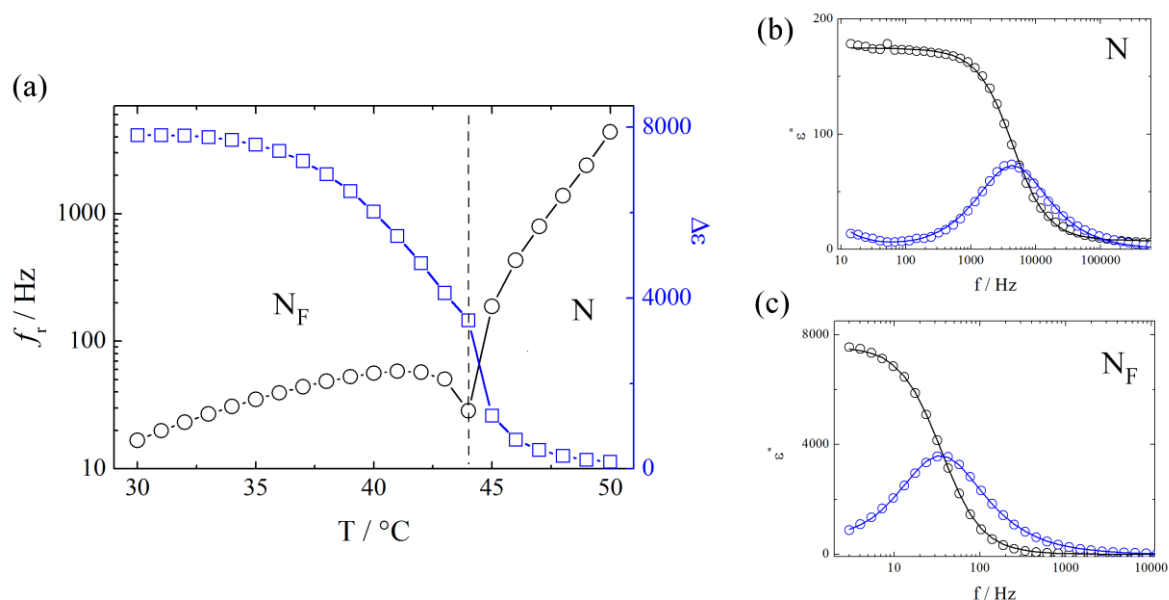


**Figure S10.** (a) Temperature dependence of relaxation frequency,  $f_r$  (black) and dielectric strength,  $\Delta\epsilon$  of the mode (blue) for compound **I-6** in 10- $\mu\text{m}$ -thick cell with Au electrodes and no aligning layers. (b) and (c) Examples of the fitting of the complex dielectric permittivity dispersion to Cole-Cole formula, in  $N$  ( $T = 50$  °C) and  $N_F$  ( $T = 35$  °C) phases. Circles are measured, real (black) and imaginary (blue) parts of dielectric permittivity, lines represent fitted curves.

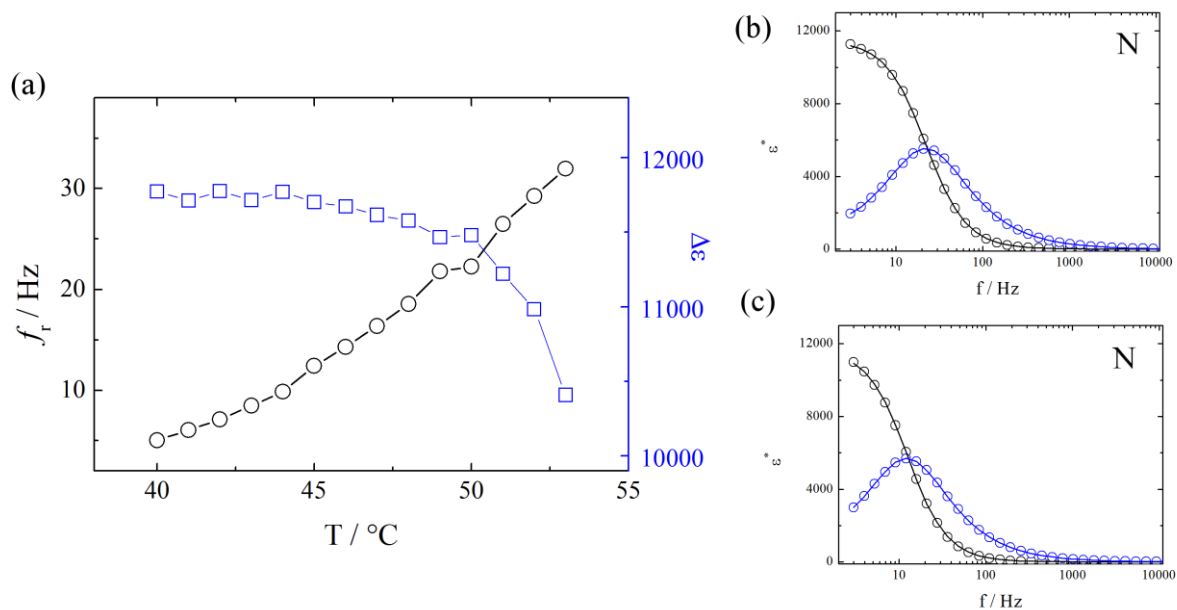


**Figure S11.** (a) Temperature dependence of relaxation frequency,  $f_r$  (black) and dielectric strength,  $\Delta\epsilon$  of the mode (blue) for compound **I-4\*** in 10- $\mu\text{m}$ -thick cell with ITO electrodes and no aligning layers. (b) and (c) Examples of the fitting of the complex dielectric permittivity dispersion to Cole-Cole formula, at  $T = 50 ^\circ\text{C}$  and  $T = 45 ^\circ\text{C}$ . Circles are measured, real (black) and imaginary (blue) parts of dielectric permittivity, lines represent fitted curves.

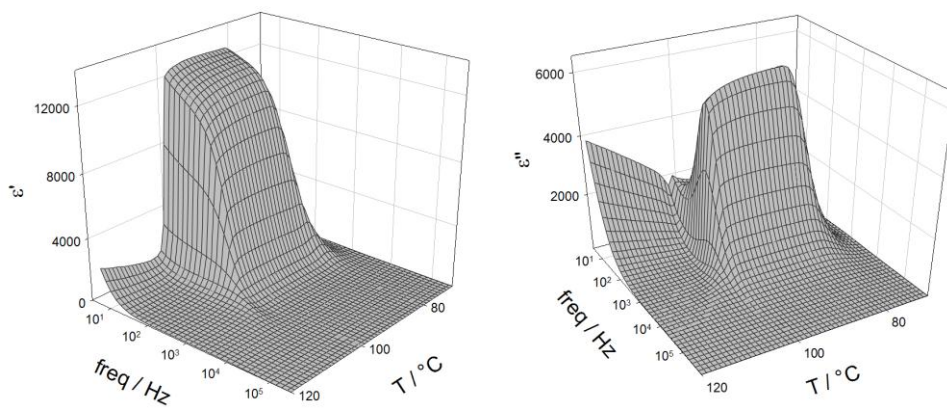


**Figure S12.** Real and imaginary part of dielectric permittivity measured vs. temperature and frequency, in 10- $\mu\text{m}$ -thick cell with ITO electrodes and no aligning layers for **I-2**.

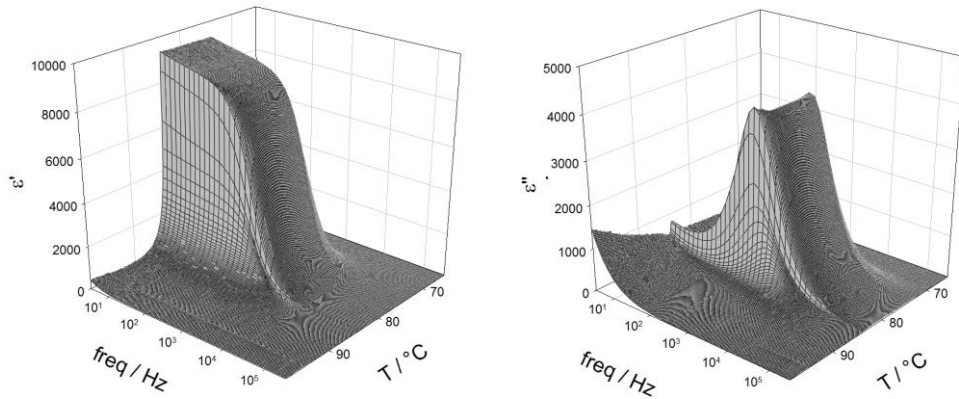


**Figure S13.** Real and imaginary part of dielectric permittivity measured vs. temperature and frequency, in 10- $\mu$ m-thick cell with ITO electrodes and no aligning layers for I-3

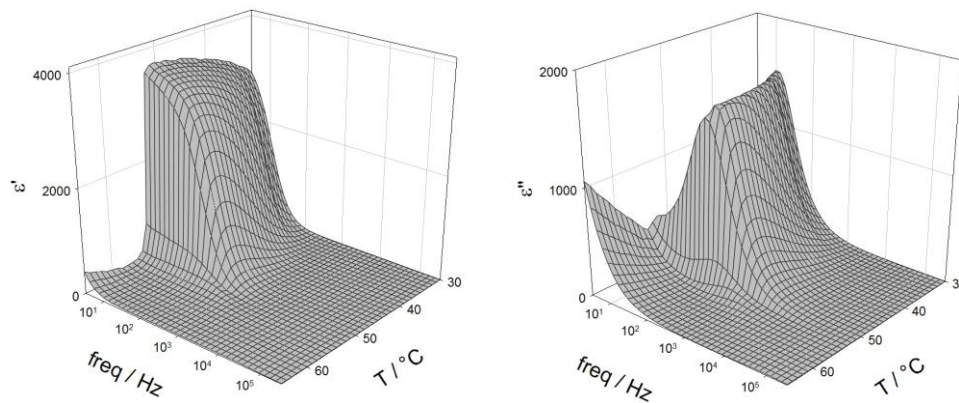


**Figure S14.** Real and imaginary part of dielectric permittivity measured vs. temperature and frequency, in 10- $\mu$ m-thick cell with ITO electrodes and no aligning layers for I-5

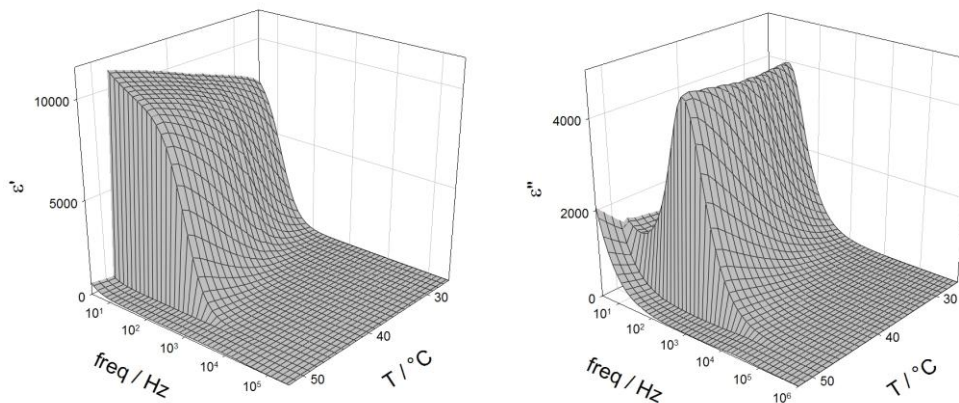


**Figure S15.** Real and imaginary part of dielectric permittivity measured vs. temperature and frequency, in 5- $\mu$ m-thick cell with Au electrodes and no aligning layers for II-6.



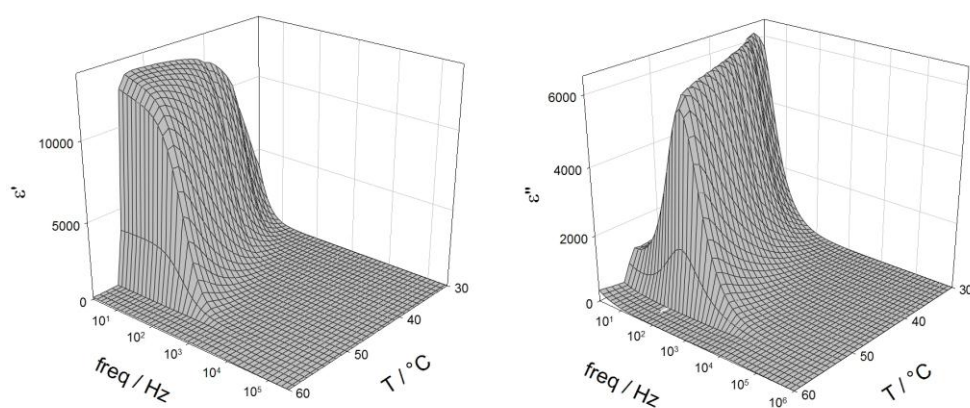


**Figure S16.** Real and imaginary part of dielectric permittivity measured vs. temperature and frequency, in 5- $\mu\text{m}$ -thick cell with Au electrodes and no aligning layers for **I-4\***.

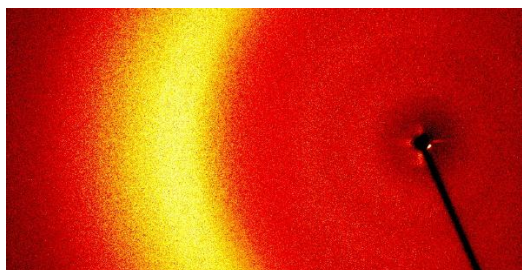


**Figure S17.** 2D X-ray diffraction pattern for compound **I-4\*** in  $N^*_F$  phase at room temperature. The diffused signals, evidencing fully fluidic nature of the phase correspond to periodicities 18.2; 9.5 and 4.5 Å.

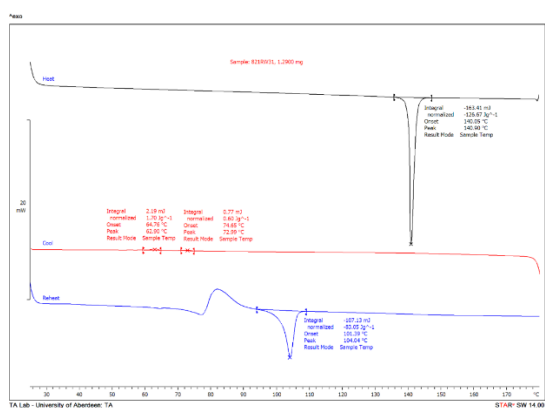


**Figure S18.** DSC curve for compound **I-4**

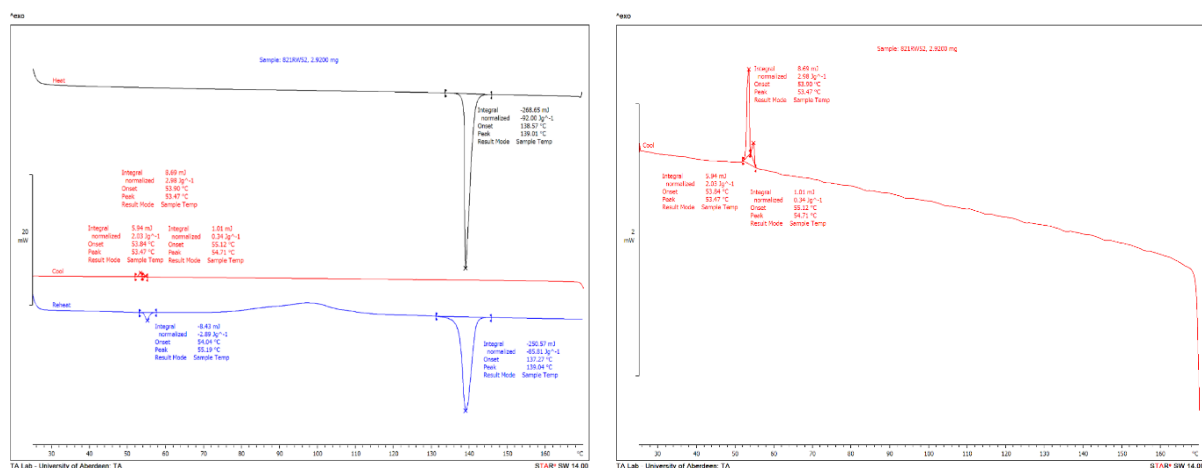


**Figure S19.** DSC curve for compound I-4\* (left - magnified part of the thermogram showing Iso-N\*-N<sub>F</sub>\* transitions)

## 5. References

- [1] X. Chen, E. Korblova, D. Dong, X. Wei, R.F. Shao, L.H. Radzihovsky, M.A. Glaser, J.E. Maclennan, D. Bedrov, D.M. Walba, N.A. Clark *First-Principles Experimental Demonstration of Ferroelectricity in a Thermotropic Nematic Liquid Crystal: Spontaneous Polar Domains and Striking Electro-Optics*, PNAS, **2020**, 117 (25), 14021-14031.
- [2] CrysAlisPro 1.171.38.43d (Rigaku OD), **2015**.
- [3] G. Sheldrick, *A short history of SHELX*, Acta Crystallographica Section A, **2008**, 64, 112-122.
- [4] G. Sheldrick, Acta Crystallographica Section C, **2015**, 71, 3-8.
- [5] O.V. Dolomanov, L.J. Bourhis, R.J. Gildea, J.A.K. Howard, H. Puschmann, *OLEX2: a complete structure solution, refinement and analysis program*, Journal of Applied Crystallography, **2009**, 42, 339-341.
- [6] X. Chen, Z. Zhu, M. J. Magrini, E. Korblova, C. S. Park, M. A. Glaser, J. E. Maclennan, D. M. Walba, N.A. Clark, **2021**, arXiv:2110.10826.
- [7] R. Saha, P. Nepal, C. Feng, M. S. Hossein, J. T. Gleeson, S. Sprunt, R. J. Twieg, A. Jakli, **2021**, arXiv:2104.06520.